

ALMA MATER STUDIORUM · UNIVERSITÀ DI BOLOGNA
UNIVERSITÉ CLERMONT AUVERGNE
TECHNISCHE UNIVERSITÄT DORTMUND

International Master in Advanced Methods in Particle Physics

Higgs boson properties and tau lepton
identification at the $\sqrt{s} = 3$ TeV
Muon Collider

Supervisor:
Prof. Michele Gallinaro

Presented by:
Lorenzo Valla

Co-supervisor:
Prof. Maximiliano Sioli

Academic Year 2023/2024

Abstract

The Higgs sector of the Standard Model (SM) is of critical importance in high energy particle physics, as the Higgs boson H could couple with new particles and provide a portal to New Physics (NP). Amongst other future colliders currently under study, a Higgs factory such as the Muon Collider would allow to perform unprecedented precision measurements of the Higgs boson parameters. The goal of this thesis is to extract an estimate of the statistical uncertainty on the cross section of the $H \rightarrow \tau^+\tau^-$ process at a 3 TeV center-of-mass energy Muon Collider. In this study, the performance of the TAUFinder algorithm, used to reconstruct τ leptons in their different decay modes through their decay products, is also assessed. An analysis of the pion track and particle reconstruction efficiencies is carried out to find an optimal event reconstruction configuration, aiming at balancing reconstruction efficiency and computational performance. The study of TAUFinder's performance demonstrates that the reconstruction efficiency of 1-prong hadronic τ leptons decays is above 60% in the detector central region ($|\eta| < 0.5$) for $10 \text{ GeV}/c \leq p_T \leq 100 \text{ GeV}/c$, where most τ leptons resulting from Higgs decay are produced. The energy corrections of the τ leptons are also computed.

The signal process $H \rightarrow \tau^+\tau^-$ is investigated, with a focus on the case of both τ leptons decaying hadronically (τ_h). The main background processes are discussed and compared with the signal. A Multivariate Analysis technique is applied to enhance the signal-background discrimination: a Boosted Decision Tree (BDT) classifier is trained using kinematical variables of the final state τ_h leptons from signal and background samples. With the resulting BDT response distributions, histogram template fits are performed in 100k Monte Carlo toy experiments, to extract an estimate of the statistical sensitivity on the cross section of the signal process: $\Delta\sigma/\sigma(H \rightarrow \tau^+\tau^-) = 5.3\%$. Finally, further steps towards improving the sensitivity to the process are discussed.

Contents

Introduction	1
1 Higgs physics	3
1.1 The Higgs boson in the Standard Model	3
1.2 Higgs properties at LHC	4
1.3 Prospect of Higgs measurements at future colliders	9
2 The Muon Collider	13
2.1 Why colliding muons?	13
2.2 Overview of the facility	16
2.2.1 Production and cooling	17
2.2.2 Acceleration	19
2.2.3 Collision	20
3 Experimental apparatus and event reconstruction	21
3.1 Collision environment	21
3.1.1 The Detector	21
3.1.2 BIB characterisation and mitigation strategies	26
3.2 Physics objects reconstruction	28
3.2.1 Software and simulations	28
3.2.2 Track reconstruction	30
3.2.3 PandoraPFA	32
4 Tau lepton reconstruction and identification	35
4.1 The tau lepton in the Standard Model	35
4.2 Tau leptons at high energy colliders	36
4.3 Charged pion reconstruction	38
4.4 Tau lepton reconstruction	42
4.4.1 The TauFinder algorithm	42
4.4.2 TauFinder performance	43
4.4.3 Tau misidentification	45

4.4.4	Tau energy corrections	47
5	$H \rightarrow \tau\tau$ process and cross section measurement	49
5.1	Signal and Background Modeling	49
5.1.1	Signal process	49
5.1.2	Background processes	50
5.2	Signal-background discrimination	52
5.2.1	Sample generation and event selection	52
5.2.2	Boosted Decision Tree	54
5.3	Fit procedure and result	57
5.4	Discussion	58
	Conclusions and outlook	61
A	Tau lepton reconstruction and identification at the CMS experiment	63
A.1	Tau reconstruction at CMS	63
A.2	Hadronic tau identification at CMS	64
B	Background processes diagrams	67
	Bibliography	69
	Acknowledgements (Ringraziamenti)	75

Introduction

The understanding of the fundamental particles and interactions that govern the functioning of the Universe is at the core of modern particle physics. The study of the Higgs boson, a cornerstone of the Standard Model (SM), is critical in this quest, since this particle plays a crucial role in the mass generation mechanism. The investigation of the Higgs boson properties, such as the precision measurements of the Higgs boson couplings to the other SM particles, is essential not only to validate the SM, but also in searching for New Physics (NP). To perform ever more precise measurements, increasingly sophisticated experiments are required. Amongst the future colliders under study, the Muon Collider stands out as a cutting-edge machine with exceptional features, as it will collide muons and antimuons at the multi-TeV scale with a relatively compact setup and a clean experimental environment (compared to proton-proton colliders). This makes it one of the most promising experiments to delve deep into the Higgs sector in search for NP.

This thesis focuses on harnessing the potential of a 3 TeV center-of-mass energy Muon Collider as a Higgs factory, especially with regard to the precise measurement of the cross section of the $H \rightarrow \tau^+\tau^-$ decay channel, i.e. the Higgs decay into a pair of τ leptons. This work also represents the first analysis of τ lepton reconstruction using the full event simulation at the Muon Collider, a central aspect in the identification of such process. In Chapters 1 to 3, the foundations of this thesis are laid by introducing the Higgs boson and its relevance in modern particle physics (Chapter 1), the Muon Collider and its physics potential (Chapter 2), its experimental apparatus and physics objects reconstruction algorithms (Chapter 3). The core of the original work is discussed in Chapters 4 and 5. In Chapter 4, a detailed characterisation of the TAU-FINDER algorithm, designed to reconstruct τ s at lepton colliders, is presented. The performance of the algorithm is assessed in different regions of the phase space with the use of simulated charged pion and τ guns. In Chapter 5, the identification of the $H \rightarrow \tau_h\tau_h$ decay process at the Muon Collider is discussed. This work marks the first time that this decay channel is studied using a full event simulation and reconstruction with the Muon Collider software MARLIN. In the analysis, TAU-FINDER is used to reconstruct τ leptons in simulated signal events. A signal-background discrimination is performed with a multivariate analysis, pivoting on kinematic variables with a high discrimination power, such as the invariant

mass of the $\tau^+\tau^-$ pair and angular distributions.

In summary, this thesis aims to assess of the status of τ lepton reconstruction at a 3 TeV Muon Collider with the TAUFinder algorithm, and to place a landmark in the $H \rightarrow \tau^+\tau^-$ decay channel measurements, suggesting possible improvements and pathways to achieve unprecedented precision measurements of the Higgs coupling to τ leptons.

Chapter 1

Higgs physics

This first chapter aims to introduce the properties of the Higgs boson and its importance in the Standard Model and in modern particle physics. The production and decay modes of the Higgs are discussed, along with the experimental measurements of its parameters and couplings at the LHC. Finally, the current perspectives of Higgs measurements at a next generation of colliders are discussed, underscoring the potential of the Muon Collider in exploring the Higgs sector and the coupling of the Higgs boson to τ leptons.

1.1 The Higgs boson in the Standard Model

The Higgs boson (H) is a cornerstone of the Standard Model of particle physics, the theory that as of today is used to describe the fundamental particles and interactions of nature. In the SM, the Higgs boson is a CP-even scalar (i.e. spin 0) particle with no electromagnetic charge. Its existence is key in the SM theory, since it allows the gauge bosons W^\pm and Z to be massive without breaking the $U(1)_Y \times SU(2)_L$ local gauge symmetry of the electroweak sector. This is achieved through a spontaneous symmetry breaking of the Higgs potential, known as the Brout–Englert–Higgs mechanism [1], which gives rise to the Higgs boson and to three Goldstone bosons. These latter provide the longitudinal degrees of freedom, and hence the masses, of the W^+ , W^- and Z bosons, without breaking the gauge symmetry. The SM Lagrangian of the Higgs sector includes therefore $\mathcal{L}_{H,\text{self}}$, a H self-interaction term, and $\mathcal{L}_{H,\text{kin}}$, a kinetic term containing the interactions of the H with the W_μ and Z_μ gauge fields:

$$\mathcal{L}_{H,\text{self}} = -\frac{m_H^2}{2}H^2 - \lambda v H^3 - \frac{\lambda}{4}H^4, \quad \text{with } m_H^2 = 2\lambda^2 v; \quad (1.1)$$

$$\mathcal{L}_{H,\text{kin}} = -\frac{1}{2}\partial^\mu H\partial_\mu H - \left(1 + \frac{H}{v}\right)^2 \left[\frac{m_W^2}{2}W_\mu^\dagger W^\mu + \frac{m_Z^2}{2}Z_\mu Z^\mu \right], \quad (1.2)$$

with $m_W^2 = \frac{1}{4}g^2v^2$, $m_Z^2 = \frac{1}{4}v^2(g'^2 + g^2)$.

This sector is described by 4 free parameters: g and g' are the electroweak couplings respectively to the $\text{SU}(2)_L$ and $\text{U}(1)_Y$ symmetry groups, λ is the Higgs quartic coupling and v is the vacuum expectation value of the Higgs potential.

The Higgs boson also appears in another part of the SM Lagrangian, the Yukawa term \mathcal{L}_{Yuk} ; this describes the interactions of the fermionic fields ψ_i with the Higgs. Writing the term in the mass basis:

$$\mathcal{L}_{\text{Yuk}} = -\sum_i m_i \left(1 + \frac{H}{v}\right) \bar{\psi}_i \psi_i, \quad \text{with } m_i = y_i \frac{v}{\sqrt{2}}, \quad (1.3)$$

where the i index runs over all the massive fermions, m_i is the mass of the fermion and y_i is called the Yukawa coupling of the fermion.

All mass terms in the SM (see Eq. 1.2 and 1.3) are generated by the Higgs field, whose couplings to the particles determine the values of the masses. Moreover, all masses are proportional to the vacuum expectation value v , along which other parameters appear: for the fermions y_i , for the bosons g and g' , for the Higgs the quartic coupling λ . In the case of the fermions, therefore, the coupling with the Higgs is proportional to the fermion's mass m_i .

1.2 Higgs properties at LHC

The Higgs boson was first observed experimentally in 2012 by the CMS [2] and ATLAS [3] collaborations at the LHC, a Multi-TeV proton-proton collider in Geneva, Switzerland. From that moment on, the two collaborations have been leading the studies on the Higgs boson properties.

Given the composite nature of the protons, at LHC the cross sections of the different H production modes are determined both by the proton-proton collision energy (also denoted with \sqrt{s}) and by the parton distribution functions (PDFs) [4] of the proton. The SM cross sections of the main production modes at a 7, 8, 13 and 14 TeV p-p collider are reported in Table 1.1, along with the total H production cross section. The gluon fusion (ggF) is the dominant process, followed by VBF, Higgs-strahlung and $t\bar{t}H$ associated production.

The Higgs boson, with a width $\Gamma_H \sim 4$ MeV [5], is an unstable particle. Its SM branching ratios (BRs) are reported in Table 1.2. As highlighted in Section 1.1, the coupling y_i of the Higgs to a fermion is proportional to the mass of the fermion m_i , hence the larger

m_i , the larger its partial width Γ_i . Note that, since $m_H < 2m_W < 2m_Z < 2m_t$, it is not possible for the Higgs to decay into W^+W^- , ZZ or $t\bar{t}$ pairs, but at least one of the two particles has to be off-shell (denoted by *). The main decay mode is therefore $H \rightarrow b\bar{b}$, followed by $H \rightarrow WW^*$, $H \rightarrow gg$ (mediated by a virtual t quark loop) and $H \rightarrow \tau^+\tau^-$.

\sqrt{s} (TeV)	Production cross section (in pb) for $m_H = 125$ GeV					
	ggF	VBF	WH	ZH	$t\bar{t}H$	total
7	$16.9^{+5.5\%}_{-7.6\%}$	$1.24^{+2.2\%}_{-2.2\%}$	$0.58^{+2.2\%}_{-2.3\%}$	$0.34^{+3.1\%}_{-3.0\%}$	$0.09^{+5.6\%}_{-10.2\%}$	19.1
8	$21.4^{+5.4\%}_{-7.6\%}$	$1.60^{+2.1\%}_{-2.1\%}$	$0.70^{+2.1\%}_{-2.2\%}$	$0.42^{+3.4\%}_{-2.9\%}$	$0.13^{+5.9\%}_{-10.1\%}$	24.2
13	$48.6^{+5.6\%}_{-7.4\%}$	$3.78^{+2.1\%}_{-2.1\%}$	$1.37^{+2.0\%}_{-2.0\%}$	$0.88^{+4.1\%}_{-3.5\%}$	$0.50^{+6.8\%}_{-9.9\%}$	55.1
14	$54.7^{+5.6\%}_{-7.4\%}$	$4.28^{+2.1\%}_{-2.1\%}$	$1.51^{+1.8\%}_{-1.9\%}$	$0.99^{+4.1\%}_{-3.7\%}$	$0.61^{+6.9\%}_{-9.8\%}$	62.1

Table 1.1: SM cross sections of the Higgs boson main production modes at a 7, 8, 13 and 14 TeV LHC, computed for $m_H = 125$ GeV [6, 7, 8].

Decay mode	BR = Γ_i/Γ_H	Rel. uncertainty
$H \rightarrow b\bar{b}$	58.2%	$+1.2\%$ -1.3%
$H \rightarrow WW^*$	21.4%	$\pm 1.5\%$
$H \rightarrow gg$	8.19%	$\pm 3.4\%$
$H \rightarrow \tau^+\tau^-$	6.27%	$\pm 1.6\%$
$H \rightarrow c\bar{c}$	2.89%	$+5.5\%$ -2.0%
$H \rightarrow ZZ^*$	2.62%	$\pm 1.5\%$
$H \rightarrow \gamma\gamma$	2.27×10^{-3}	$\pm 2.1\%$
$H \rightarrow Z\gamma$	1.53×10^{-3}	$\pm 5.8\%$
$H \rightarrow \mu^+\mu^-$	2.18×10^{-4}	$\pm 1.7\%$

Table 1.2: Main SM branching ratios of the Higgs boson and relative theoretical uncertainties for $m_H = 125$ GeV [7, 8]. The $H \rightarrow gg$ decay is mediated by a loop of (mainly) virtual top quarks, while the $H \rightarrow \gamma\gamma$ and $H \rightarrow Z\gamma$ decays are mediated either by a loop of virtual W bosons or top quarks.

Despite their low partial widths, the H decay channels that led to the first Higgs observation in [2] and [3] are $H \rightarrow \gamma\gamma$ and $H \rightarrow ZZ^* \rightarrow 4\ell$, given their clean signature in the experimental apparatus. The same channels were used by the CMS and ATLAS experiments to measure the Higgs boson mass at a per-mille level precision with the LHC Run 1 and Run 2 data. The current most precise measurement of the Higgs mass is $m_H = (125.11 \pm 0.11) \text{ GeV}$ [9], shown in Figure 1.1, performed by ATLAS by combining the results in the di-photon and 4ℓ decay channels. The current most precise measurement in a single decay channel is instead $m_H = (125.08 \pm 0.12) \text{ GeV}$ [10], obtained by CMS in the 4ℓ decay channel.

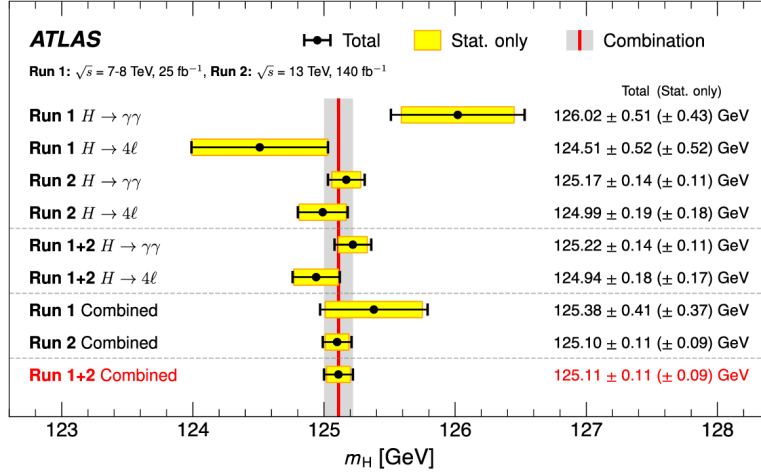


Figure 1.1: ATLAS measurements of the Higgs boson mass in the $H \rightarrow \gamma\gamma$ and $H \rightarrow ZZ^* \rightarrow 4\ell$ decay channels, performed with LHC Run 1 and Run 2 data. Taken from Ref. [9].

In the so-called κ framework, the couplings of the Higgs boson to other particles are usually parametrized with the coupling modifiers $\kappa_i \equiv g_i/g_i^{\text{SM}}$, i.e. the ratio between the measured Higgs coupling to the particle i and the coupling predicted by the SM. The value $\kappa_i = 1$ expresses a perfect agreement with the SM predictions. Given a $i \rightarrow H \rightarrow f$ process of initial state i and final state f , and using the small width approximation ($\Gamma_H \ll m_H$), the signal strength of the process relative to the SM expectations may be written as

$$\begin{aligned} \mu_i^f &\equiv \frac{\sigma(i \rightarrow H) \cdot \text{BR}(H \rightarrow f)}{\sigma(i \rightarrow H)_{\text{SM}} \cdot \text{BR}(H \rightarrow f)_{\text{SM}}} = \\ &= \frac{\sigma_i \Gamma_f / \Gamma_H}{\sigma_i^{\text{SM}} \Gamma_f^{\text{SM}} / \Gamma_H^{\text{SM}}} = \end{aligned}$$

$$\begin{aligned}
&= \frac{(1 + \kappa_i^2)\sigma_i^{\text{SM}}(1 + \kappa_f^2)\Gamma_f}{\sigma_i^{\text{SM}}\Gamma_f^{\text{SM}}} \cdot \frac{1/\Gamma_H}{1/\Gamma_H^{\text{SM}}} = \\
&= \frac{\kappa_i^2\sigma_i^{\text{SM}} \cdot \kappa_f^2\Gamma_f^{\text{SM}}}{\Gamma_H/\Gamma_H^{\text{SM}}} = \\
&= \frac{\kappa_i^2 \cdot \kappa_f^2}{\kappa_H^2} (1 - \text{BR}_{\text{BSM}}) , \tag{1.4}
\end{aligned}$$

where BR_{BSM} is the branching ratio of the Higgs decaying into particles beyond the SM (BSM), and κ_H is a modifier that adjusts the Higgs width to take into account the other κ_i modifiers:

$$\kappa_H = \sum_j \frac{\kappa_j^2 \Gamma_j^{\text{SM}}}{\Gamma_H^{\text{SM}}} . \tag{1.5}$$

It is crucial to remark that the signal strength might be affected by the presence of NP processes, such as the Higgs decaying into BSM particles. These hypothetical decays can be separated in two classes: decays into invisible particles, which are experimentally directly constrained at colliders (BR_{inv}), and decays into BSM final states that are undetectable with the current experimental setups¹ (BR_{undet}), that yield $\text{BR}_{\text{BSM}} = \text{BR}_{\text{inv}} + \text{BR}_{\text{undet}} \neq 0$. The present status of the coupling modifiers measurements in the $\text{BR}_{\text{BSM}} = 0$ scenario at CMS is reported in Figure 1.2.

The measurement of the Higgs self-couplings, which determine the shape of the Higgs potential (see Equation 1.1), has yet to be performed. According to the SM, the predicted values of the trilinear and quadrilinear self-couplings are respectively $\lambda_3 = \lambda v$ and $\lambda_4 = \lambda/4$. The value of v and λ can be extracted from muon decay and m_H measurements, to have a precise prediction of the self-couplings values. The major challenge in measuring λ_3 (and even more λ_4) at the LHC is the tiny cross section of the processes under investigation: $\sigma(pp \rightarrow HH) \sim 33 \text{ fb}$ at $\sqrt{s} = 13 \text{ TeV}$ [13]. Alternatively, the trilinear self-coupling can be indirectly constrained through loop-induced corrections to the single Higgs boson production. Limits on the trilinear self-coupling modifier $\kappa_\lambda = \lambda_3/\lambda_3^{\text{SM}}$, combining direct HH production searches and indirect single- H constraints, were set by the ATLAS and CMS experiments²: $-0.4 < \kappa_\lambda < 6.3$ at 95% CL (ATLAS, Ref. [13]) and $-1.2 < \kappa_\lambda < 7.5$ at 95% CL (CMS, Ref. [14]).

All the measurements of the Higgs boson parameters performed so far have shown no discrepancy with respect to the SM expectations. Nonetheless, the precision on many decay and production modes is not enough to rule out New Physics. Moreover, the Higgs

¹For example, a Higgs decaying to light hadrons, as in Ref. [11].

²The results quoted here assume that New Physics only affects the H self-coupling; for more details, see Refs. [13, 14].

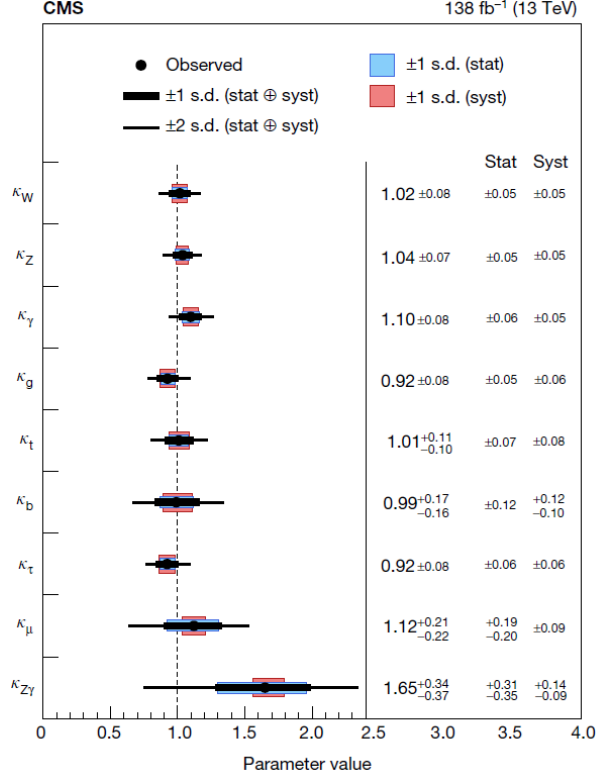


Figure 1.2: Status of the Higgs coupling modifiers for SM particles as obtained from a fit on Run 2 data by the CMS experiment, assuming $\text{BR}_{\text{BSM}} = 0$. Taken from Ref. [12].

self-interactions and some production and decay processes have yet to be observed. Many New Physics models predict deviations of the Higgs branching ratios and self-couplings from the expected SM values. According to the Higgs Portal paradigm [15], the Higgs could couple (or even mix) with fields not belonging to the Standard Model, including Dark Matter particles. A better knowledge of the Higgs parameters is required to confirm or dismiss such theories. Furthermore, the Higgs boson is related to many other open questions in the SM, such as the hierarchy problem and the stability of the vacuum [16].

These are amongst the main motivations for planning and building a Higgs factory, i.e. a next-generation collider able to produce Higgs bosons at a very high rate and perform precision measurements of its parameters and couplings, in order to explore in depth the Higgs sector and hunt for discrepancies with respect to the Standard Model predictions.

1.3 Prospect of Higgs measurements at future colliders

Many colliders have been proposed by the scientific community to investigate the Higgs sector and look for NP. One of them is the Muon Collider, the $\mu^+\mu^-$ machine that is the subject of this thesis and whose characteristics are described in Chapter 2. The other most prominent ones are the following:

- High Luminosity Large Hadron Collider (HL-LHC) [17], an upgrade of the current LHC that will be studying proton-proton collisions at $\sqrt{s} = 14$ TeV, with an expected increase in the integrated luminosity of a factor 10 with respect to the LHC design value. The huge statistics provided by the machine will allow to improve the precision on several Higgs parameters. The collider project has already been approved, and it is foreseen to start the data-taking phase in 2029.
- Future Circular Collider (FCC) [18], a circular collider for which three possible modes of operation are envisaged: an electron-positron (FCC-ee), hadron-hadron (FCC-hh) or electron-hadron (FCC-eh) machine. Each of these colliders would have its unique characteristics: FCC-ee could serve as a Higgs factory, exploiting the clean experimental environment to perform precision measurements of the Higgs boson mass and its branching ratios; FCC-hh could reach center-of-mass energies up to 100 TeV, far beyond the current machines, and be able to probe the trilinear and quadrilinear Higgs self-couplings; FCC-eh (with a 60 GeV e^- and a 50 TeV p beams) could explore the Higgs self-interactions as well as probe hidden sectors via the Higgs portal.
- Circular Electron Positron Collider (CEPC) [19], a circular e^+e^- machine designed to operate as a $\sqrt{s} = 240$ GeV Higgs factory, producing more than one million H bosons via $e^+e^- \rightarrow HZ$ (Higgs-strahlung).
- International Linear Collider (ILC) [20], a linear e^+e^- collider able to easily change its energy in the center of mass. Three possible stages are under study: the first at $\sqrt{s} = 250$ GeV, to perform Higgs precision measurements and be sensible to invisible or exotic Higgs decays; the second one at $\sqrt{s} = 500$ GeV, which would allow to probe Higgs self-couplings and top-Higgs interactions; a final stage at $\sqrt{s} = 1$ TeV. A linear collider such as ILC would be capable of producing polarized e^+ and e^- beams, to produce new observables inaccessible at LHC.
- Compact Linear Collider (CLIC) [21], a linear e^+e^- machine with higher center-of-mass energies than ILC: $\sqrt{s} = 380$ GeV, 1.5 TeV and 3 TeV in three different stages. The 380 GeV collider would allow precision studies in the of the Higgs parameters and of $H \rightarrow$ invisible, while the higher energies would probe the Higgs

self-interactions, the $H\bar{t}t$ channel and Higgs exotic decay channels. Given the capability of producing polarized e^- beams, all three stages would give access to new angular observables.

Collider	Type	\sqrt{s}	$\mathcal{P}[\%]$ [e^-/e^+]	N(Det.)	$\mathcal{L}_{\text{inst}}$ [10^{34}]cm $^{-2}$ s $^{-1}$	\mathcal{L} [ab $^{-1}$]	Time [years]
HL-LHC	pp	14 TeV	-	2	5	6.0	12
FCC-hh	pp	100 TeV	-	2	30	30.0	25
FCC-ee	ee	M_Z	0/0	2	100/200	150	4
		$2M_W$	0/0	2	25	10	1-2
		240 GeV	0/0	2	7	5	3
		$2m_{\text{top}}$	0/0	2	0.8/1.4	1.5	5 (+1)
ILC	ee	250 GeV	$\pm 80/\pm 30$	1	1.35/2.7	2.0	11.5
		350 GeV	$\pm 80/\pm 30$	1	1.6	0.2	1
		500 GeV	$\pm 80/\pm 30$	1	1.8/3.6	4.0	8.5
		1000 GeV	$\pm 80/\pm 20$	1	3.6/7.2	8.0	8.5 (+1-2)
CEPC	ee	M_Z	0/0	2	17/32	16	2
		$2M_W$	0/0	2	10	2.6	1
		240 GeV	0/0	2	3	5.6	7
CLIC	ee	380 GeV	$\pm 80/0$	1	1.5	1.0	8
		1.5 TeV	$\pm 80/0$	1	3.7	2.5	7
		3.0 TeV	$\pm 80/0$	1	6.0	5.0	8 (+4)
FCC-eh	ep	3.5 TeV	-	1	1.5	2.0	25

Table 1.3: Operational parameters of the main future colliders proposed. \mathcal{P} denotes the polarization degree of the e^-/e^+ beams, N is the number of interaction points where detectors would be placed, $\mathcal{L}_{\text{inst}}$ is the instantaneous luminosity, \mathcal{L} the integrated luminosity accumulated in the time reported alongside it. The years within brackets refer to the duration of shutdowns for detector and infrastructure upgrades. Taken from Ref. [22].

A summary of the running conditions of these colliders is reported in Table 1.3 (the parameters of the MuCol are available in Section 2.2), while the projected relative uncertainties achievable on the different coupling modifiers (in the $\text{BR}_{\text{BSM}} = 0$ scenario) are shown in Table 1.4.

Considering the κ_τ coupling modifier, of particular importance in this work, a significant increase in sensitivity can be noticed when comparing the projection of many future colliders compared to the current value of $\sim 8\%$ obtained at CMS (see Figure 1.2) and ATLAS [25]. Specifically, a 10 TeV MuCol is projected to set one of the most stringent limit on the κ_τ uncertainty, providing an excellent insight on the H coupling to the τ leptons.

Coupling	HL-LHC	ILC			CLIC			CEPC	FCC-ee		FCC	MuCol	
		250	500	1000	380	1500	3000		240	365		3 TeV	10 TeV
κ_W [%]	1.7	1.8	0.29	0.24	0.86	0.16	0.11	1.3	1.3	0.43	0.14	0.55	0.16
κ_Z [%]	1.5	0.29	0.23	0.22	0.5	0.26	0.23	0.14	0.20	0.17	0.12	5.1	1.4
κ_g [%]	2.3	2.3	0.97	0.66	2.5	1.3	0.9	1.5	1.7	1.0	0.49	2.0	0.52
κ_γ [%]	1.9	6.7	3.4	1.9	98★	5.0	2.2	3.7	4.7	3.9	0.29	3.2	0.84
$\kappa_{Z\gamma}$ [%]	10.	99★	86★	85★	120★	15	6.9	8.2	81★	75★	0.69	24	6.5
κ_c [%]	-	2.5	1.3	0.9	4.3	1.8	1.4	2.2	1.8	1.3	0.95	6.8	2.0
κ_t [%]	3.3	-	6.9	1.6	-	-	2.7	-	-	-	1.0	35	55
κ_b [%]	3.6	1.8	0.58	0.48	1.9	0.46	0.37	1.2	1.3	0.67	0.43	0.97	0.26
κ_μ [%]	4.6	15	9.4	6.2	320★	13	5.8	8.9	10	8.9	0.41	20	4.9
κ_τ [%]	1.9	1.9	0.70	0.57	3.0	1.3	0.88	1.3	1.4	0.73	0.44	2.3	0.63

Table 1.4: Expected relative uncertainty (in %) on the κ_i parameters in the $\text{BR}_{\text{BSM}} = 0$ scenario for different future colliders, obtained from a fit on the projected measurements [22, 23]. The estimates for each experiment are independent and not combined with other colliders. For multi-stage colliders, predictions are shown separately for each E_{cm} (in GeV). The dash (-) denotes cases for which the parameter was fixed to its SM value due to the lack of sensitivity, while the star (★) indicates the cases in which a parameter has been left free in the fit due to lack of input in the reference documentation. The FCC column corresponds to the combined performance of FCC-ee₂₄₀+FCC-ee₃₆₅, FCC-eh and FCC-hh. The MuCol results assume an integrated luminosity of respectively $\mathcal{L} = 1 \text{ ab}^{-1}$ and $\mathcal{L} = 10 \text{ ab}^{-1}$ for the $\sqrt{s} = 3 \text{ TeV}$ and 10 TeV stages, and they are extracted with DELPHES [24] fast simulation with some caveats, such as the exclusion from the analysis of the beam-induced background generated by the muon decays (see Ref. [23]).

Another main goal of the future generation of experiments in particle physics is the determination of the Higgs self-couplings. As already introduced in the previous section, these have yet to be measured directly, given the tiny cross section of the processes at the colliders currently in operation. For the next-generation machines under planning, the sensitivity will hopefully be sufficient to investigate the deviations predicted by many NP models.

The trilinear coupling λ_3 is more accessible than the quadrilinear coupling λ_4 . It is possible to parametrize the deviation from its SM expectation with

$$\delta\kappa_\lambda \equiv \kappa_\lambda - 1 = \left(\frac{\lambda_3}{\lambda_3^{\text{SM}}} - 1 \right). \quad (1.6)$$

Studies have been performed to estimate the precision achievable on κ_λ at e^+e^- [26],

pp [27] and $\mu^+\mu^-$ [28] future colliders. As it is shown in Figure 1.3, a 10 TeV MuCol would be able to reach a precision on κ_λ at the level of the FCC-hh experiment, if not better. A further increase in the center-of-mass energy would allow a sensitivity far beyond the ones of the other next-generation colliders under study.

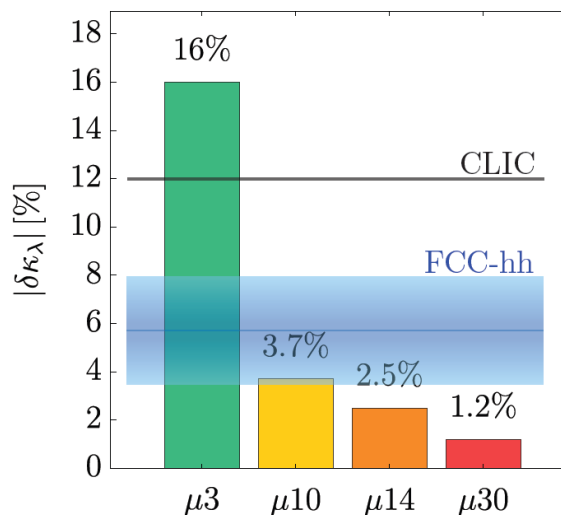


Figure 1.3: Precision reach on κ_λ at the Muon Collider for different center-of-mass energies, obtained from a fit on the projected measurements. The comparison with the performance of CLIC and FCC-hh is also shown. Taken from Ref. [28].

Chapter 2

The Muon Collider

This chapter is meant to introduce the Muon Collider program, its motivations, its physics potential and the general features and challenges of colliding muons.

The first section is dedicated to the description of the characteristics of a $\mu^+\mu^-$ collider and of the advantages of building such an experiment. Its physics potential is explored, with emphasis on the Higgs boson studies. Subsequently, a general overview of the Muon Collider program is given, based on the work of the International Muon Collider Collaboration [29]. Finally, the technologies employed in $\mu^+\mu^-$ production, cooling, acceleration and collision stages are briefly reviewed.

2.1 Why colliding muons?

The Muon Collider (MuCol) is a machine unique in its genre. Unlike all the other proposed future colliders under planning (see Section 1.3), in which the initial state particles are protons or e^+e^- , it collides muons and antimuons ($\mu^+\mu^-$). This entails both advantages and challenges.

Muons, like protons, can be made to collide at a centre-of-mass energy of the order of 10 TeV in a relatively compact ring, without fundamental limitations from synchrotron radiation, reducing the cost and the dimensions of the infrastructure. This is a consequence of the value of the muon mass ($m_\mu = 105.66 \text{ MeV}/c^2$), which leads to a significantly lower synchrotron emission compared to the much lighter electrons ($m_e = 0.511 \text{ MeV}/c^2$). At the same time, muons are leptons, so they have characteristics in common with the e^+e^- colliders: (i) the absence of partons with a QCD charge in the initial states provides a clean experimental environment in the events, not polluted by the hadronic jets background present in pp machines and caused by the large QCD interaction cross section; (ii) all the kinetic energy carried by the muons beams, acquired during the acceleration process, is used in the $\mu^+\mu^-$ collisions to produce the final states.

(iii) the energy of the initial state of the colliding particles is not dependent on any parton distribution functions (and the relative uncertainty). This makes a muon collider with a given nominal energy and luminosity more effective than a pp collider with comparable energy and luminosity (see Figure 2.1), in which the partons that do not take part in the hard scattering can carry away a significant amount of energy.

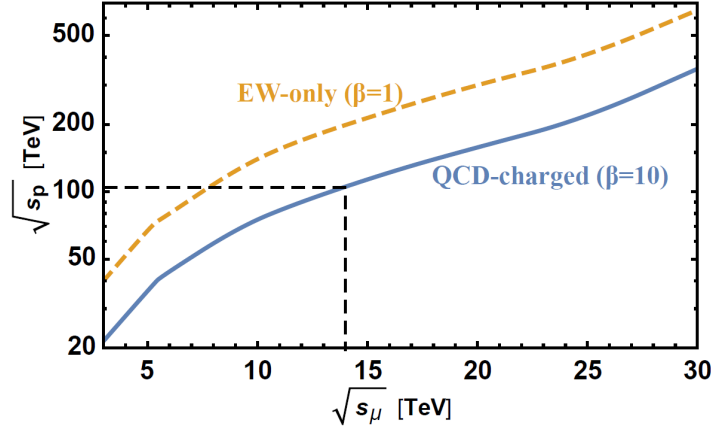


Figure 2.1: Equivalent proton collider energy, i.e. the $\sqrt{s_p}$ of a pp collider and the $\sqrt{s_\mu}$ of a muon collider for which the pair production cross section of a heavy particle with a mass close to $\sqrt{s_\mu}/2$ takes the same value. The equivalent energy depends on the relative strength β of the heavy particle coupling to partons versus muons: the orange line denotes the scenario in which the particle has only Electroweak quantum numbers and no QCD charge ($\beta = 0$), the blue line the case in which the heavy particle carries a QCD color charge with $\beta = 10$. The plot assumes that both qq and gg partonic initial states contribute to the production. Taken from Ref. [28].

Such a collider would therefore combine advantages of both the pp and the e^+e^- machines, pushing the high energy frontier in particle physics while also performing precision measurements in a clean environment. Lastly, the Muon Collider energy efficiency (in $\text{ab}^{-1}/\text{TWh}$) grows as \sqrt{s} increases; this makes a 3 or 10 TeV muon collider one of the most "environment-friendly" machine amongst the ones under study (see Section 1.3).

The MuCol is a Higgs factory, i.e. it is able produce Higgs bosons at a very high rate and perform precision measurements of the Higgs sector parameters. The production cross section of the Higgs boson in different modes is illustrated in Figure 2.2. It is important to remark that a muon collider is essentially a vector boson collider, since muons with energies above the Electroweak scale $m_W \sim 100$ GeV have a high probability of emitting W^\pm or Z bosons. This implies that at a Multi-TeV MuCol the Higgs boson production proceeds mainly via Vector Boson Fusion (Figure 2.4b and 2.4a) and Higgs-strahlung (Figure 2.4c), rather than via muon annihilation.

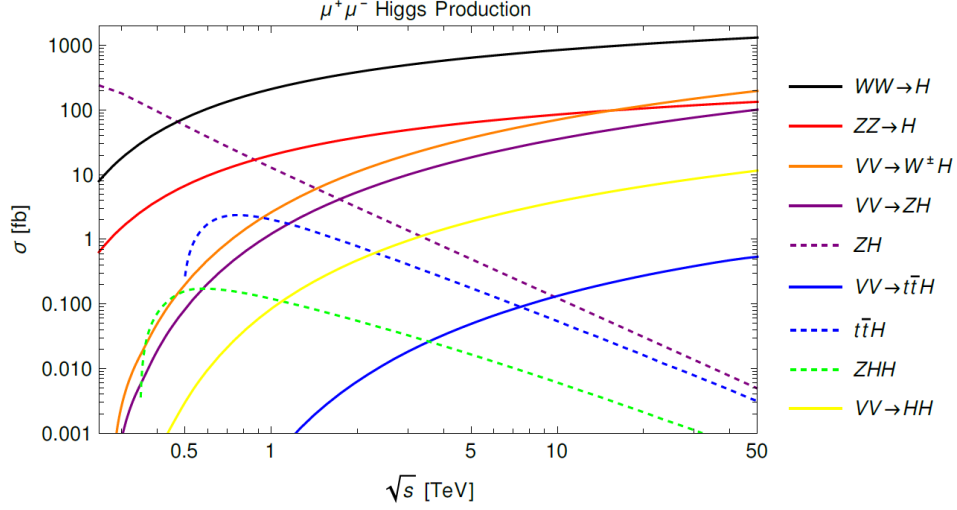


Figure 2.2: Cross sections for the main Higgs boson production processes as a function of the muon collider center-of-mass energy. The dashed line denotes production via the s -channel, the solid line production via Vector Boson Fusion. Taken from Ref. [30].

	cross section [fb]		expected events	
	3 TeV	10 TeV	1 ab ⁻¹ at 3 TeV	10 ab ⁻¹ at 10 TeV
H	550	930	5.5×10^5	9.3×10^6
ZH	11	35	1.1×10^4	3.5×10^5
$t\bar{t}H$	0.42	0.14	420	1.4×10^3
HH	0.95	3.8	950	3.8×10^4
HHH	3.0×10^{-4}	4.2×10^{-3}	0.30	42

Figure 2.3: Cross sections for the main Higgs boson production modes at $\sqrt{s} = 3$ TeV and 10 TeV and the expected events for an integrated luminosity $\mathcal{L} = 1$ ab⁻¹ and 10 ab⁻¹, respectively. Taken from Ref. [31].

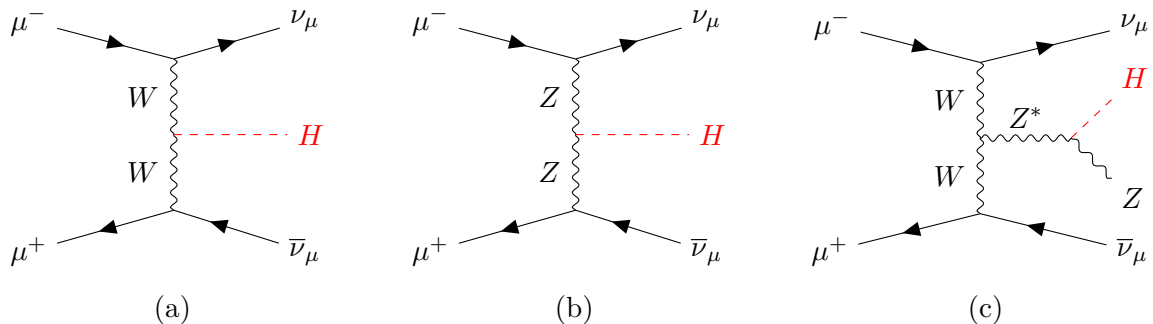


Figure 2.4: Main single H production processes at a Multi-TeV muon collider: (a) WW fusion, (b) ZZ fusion, (c) Higgs-strahlung.

Assuming an integrated luminosity of 1 ab^{-1} , at a 3 TeV MuCol approximately 500k Higgs bosons are expected to be produced (see Table 2.3): a huge statistics that would allow to measure the most important Higgs parameters with excellent precision.

Amongst the future colliders under study (see Section 1.3), the MuCol is the machine able to achieve the highest precision on most of the main Higgs parameters and couplings. Together with the characteristics listed above, this makes building a collider of this kind a unique opportunity to study in depth the Higgs sector.

All the exceptional experimental features of a muon collider come with demanding challenges: (i) R&D studies are ongoing to assess the feasibility of muon production (Section 2.2.1), cooling (Section 2.2.1) and acceleration (Section 2.2.2); (ii) magnets with a massive solenoidal field are needed in all the operational stages; (iii) there are concerns regarding possible radiation hazards caused by neutrinos (produced in muon decays and interactions) showering far from the detector facility; (iv) the impact in the detector of the beam-induced background (BIB) caused by muon decays in the beam pipe has to be reduced as much as possible. Subject (i) will be introduced in Section 2.2, while (ii) and (iii) will not be tackled here. More information about both topics can be found in [28] and [32]. Item (iv) is instead discussed in Chapter 3.

2.2 Overview of the facility

The Muon Accelerator Programme (MAP) [33] has developed a baseline concept for the design of a muon collider, which is being carried forward by the International Muon Collider Collaboration (IMCC) [29]. According to the latest IMCC plans [32], two possible MuCol scenarios are being considered: either (i) a first stage at $\sqrt{s} = 3 \text{ TeV}$ and a second stage at 10 TeV, for which the whole 3 TeV facility would be reused with the exception of the collider ring, or (ii) a first stage at 10 TeV with reduced luminosity, and a second

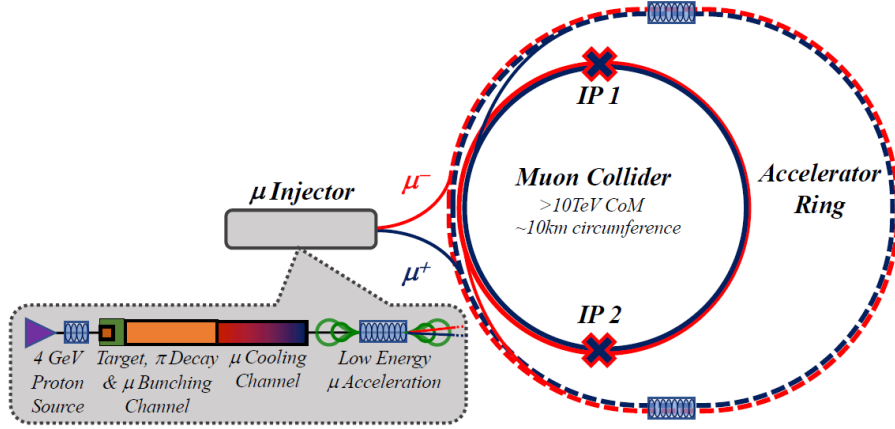


Figure 2.5: A conceptual scheme of the MuCol facility as planned by the IMCC. Taken from Ref. [28].

stage at full luminosity (the increased in luminosity would be achieved through the use of stronger magnets).

A scheme of the whole IMCC muon collider facility is depicted in Figure 2.5, while in Table 2.1 its main parameters are reported. The operational steps of such a machine are discussed in the sections below.

2.2.1 Production and cooling

One of the main challenges in running a muon collider is producing high intensity collimated muon beams with a narrow distribution in energy. This challenge is tightly related with the nature of the muons, since (i) they cannot be extracted from ordinary matter, therefore they need to be produced from decays of secondary particles; (ii) they are unstable particles, with a mean lifetime of $\tau_\mu = 2.2 \times 10^{-16}$ s in the rest frame.

To produce muons, a beam of protons (of the order of the MW) is first accelerated in a linear accelerator (LINAC) up to ~ 4 GeV, clustered in bunches of ~ 2 ns and made to impinge on a target made of e.g. graphite or liquid metal. A large number of charged pions and kaons is produced in the collision. A strong solenoidal magnetic field (15 - 20 T) along the longitudinal direction is able to capture the charged hadrons of both sign, which in turn decay to produce (anti)muons. The beam leaving the target area has a large longitudinal and transverse emittance. Therefore, the final state muons must undergo a cooling process, i.e. they need to be collimated and "slowed" to have a more uniform energy distribution, reducing their phase-space. The muons are captured and packed up into a train of bunches using Radio Frequency (RF) cavities, where slower muons are accelerated and faster muons are slowed, preparing them for the cooling stage. It is key that the cooling process proceeds as fast as possible: the lifetime of the muons

Parameter	Symbol	unit	Scenario 1		Scenario 2	
			Stage 1	Stage 2	Stage 1	Stage 2
Centre-of-mass energy	E_{cm}	TeV	3	10	10	10
Target integrated luminosity	$\int \mathcal{L}_{\text{target}}$	ab ⁻¹	1	10	10	
Estimated luminosity	$\mathcal{L}_{\text{estimated}}$	10 ³⁴ cm ⁻² s ⁻¹	2.1	21	tbc	14
Collider circumference	C_{coll}	km	4.5	10	15	15
Collider arc peak field	B_{arc}	T	11	16	11	11
Luminosity lifetime	N_{turn}	turns	1039	1558	1040	1040
Muons/bunch	N	10 ¹²	2.2	1.8	1.8	1.8
Repetition rate	f_{r}	Hz	5	5	5	5
Beam power	P_{coll}	MW	5.3	14.4	14.4	14.4
RMS longitudinal emittance	ε_{\parallel}	eVs	0.025	0.025	0.025	0.025
Norm. RMS transverse emittance	ε_{\perp}	μm	25	25	25	25
IP bunch length	σ_z	mm	5	1.5	tbc	1.5
IP betafunction	β	mm	5	1.5	tbc	1.5
IP beam size	σ	μm	3	0.9	tbc	0.9
Protons on target/bunch	N_{p}	10 ¹⁴	5	5	5	5
Protons energy on target	E_{p}	GeV	5	5	5	5
BS photons	$N_{\text{BS},0}$	per muon	0.075	0.2	tbc	0.2
BS photon energy	$E_{\text{BS},0}$	MeV	0.016	1.6	tbc	1.6
BS loss/lifetime (2 IP)	$E_{\text{BS,tot}}$	GeV	0.002	1.0	tbc	0.67

Table 2.1: Tentative target parameters of the muon collider machine according to the IMCC. The two different scenarios reported, the first with a lower energy stage and the second with a reduced luminosity stage, are described at the beginning of Section 2.2. The "tbc" labels denote parameters yet "to be calculated". Taken from Ref. [32].

produced from pion decays is dilated in the laboratory frame by the Lorentz boost, but it is important to accelerate them as soon as possible to further increase the time dilation and lose as little muons as possible. To face this challenge, an innovative cooling system has been proposed by the MICE collaboration: the ionization cooling [34].

Ionization cooling proceeds by alternating two sections with complementary functionalities. In the first section, shown in Figure 2.6, transverse ionization cooling is performed: muons are made to interact with an absorber, losing part of their energy via ionization; subsequently, they are accelerated along the longitudinal direction by some RF cavities. This is done to reduce the angular spread of the beam, while also avoiding to lose a significant amount of muons by keeping their speed high enough.

In the second section, the longitudinal emittance is reduced by exploiting the emittance exchange technique. The muons in the beam pass through an absorber for a length that is proportional to their energy: the higher energy muons travel for a longer distance in the material, losing more energy, while the lower energy muons cross a shorter portion of the absorber, losing less energy. The longitudinal emittance increases, while the position spread increases (due to a dipole magnet used to separate the energy components of the beam). This procedure, sketched in Figure 2.7, allows to obtain a beam with an energy distribution peaked around the desired value.

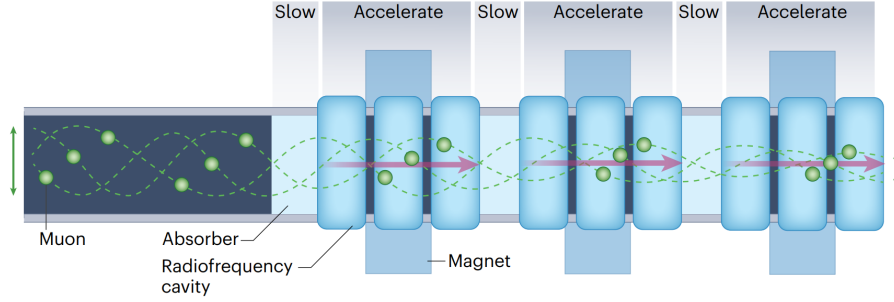


Figure 2.6: Transverse ionization cooling sketch. The muon beam incoming from the left crosses alternated layers of absorber material (e.g. liquid hydrogen) and RF cavities, that reduce the transverse emittance by increasing the longitudinal one. Taken from Ref. [35].

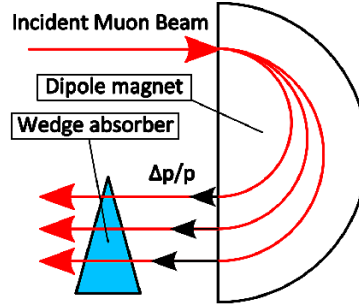


Figure 2.7: Emittance exchange technique. The incident muon beam crosses a region with a dipole magnet field, which separates the beam components based on their momenta (increasing the transverse emittance) and performs longitudinal cooling by using of a wedge absorber. Taken from Ref. [36].

Alternating the two sections allows to reduce both the transverse emittance as well as the longitudinal one, decreasing the muon beam emittance in both momentum and position spaces of 5 orders of magnitude.

2.2.2 Acceleration

After being cooled, the (anti)muon beams need to be accelerated up to the final collision energies. The baseline design for acceleration uses a series of LINACs at sub-100 GeV energies, followed by a series of pulsed synchrotrons. The RF system plays a crucial role in accelerating the low-energy incoming muon beam, while it can become costly for accelerating higher energies beams. This is circumvented by reinjecting the beam into the same Recirculating Linear Accelerator (RLA) multiple times. RLAs require a precise tuning of the geometry and a system of focus for the different energies of the beams.

Rapid Cycling Synchrotrons (RCS), pulsed synchrotrons where the magnetic fields are proportional to the beam momentum, are then used to accelerate the beam to the final energies.

2.2.3 Collision

The accelerated muon beams are injected in the collider ring, where the $\mu^+\mu^-$ interactions can produce interesting physics events whose data is then collected by the detectors. In head-on collisions, with beams of opposite charge and of Gaussian transverse distribution, the instantaneous luminosity is given by

$$\mathcal{L}_{\text{inst}} = \frac{f_{\text{coll}}}{4\pi} \frac{N^+ N^-}{\sigma_x^* \sigma_y^*}, \quad (2.1)$$

where f_{coll} is the bunch crossing frequency, N^- (N^+) is the number of μ^- (μ^+) per bunch and σ_x^* (σ_y^*) is the transverse beam size along the x (y) direction. To accumulate a high statistics, it is necessary to either increase $\mathcal{L}_{\text{inst}}$ or the data-taking time. The first one can be maximized by optimizing the cooling system to reduce the beam transverse dimensions (σ_x^*, σ_y^*), cooling and accelerating the muons faster to reduce the number of decays and increase the number of (anti)muons per bunch (N^-, N^+), using a small collision ring¹ to increase the collision frequency (f_{coll}). A target integrated luminosity can be established by considering the cross-section of a typical $2 \rightarrow 2$ scattering processes mediated by the electroweak interactions, $\sigma \sim 1 \text{ fb} \cdot (10 \text{ TeV})^2 / (E_{\text{cm}})^2$. The corresponding integrated luminosity is

$$\mathcal{L} = 10 \text{ ab}^{-1} \left(\frac{E_{\text{cm}}}{10 \text{ TeV}} \right)^2. \quad (2.2)$$

Assuming an operation time of 10^7 seconds per year and one interaction point, the target instantaneous luminosity becomes

$$\mathcal{L} = \frac{5 \text{ yrs}}{\text{time}} \left(\frac{E_{\text{cm}}}{10 \text{ TeV}} \right)^2 2 \cdot 10^{35} \text{ cm}^{-2} \text{ s}^{-1}. \quad (2.3)$$

The current design target parameters (see Table 2.1) allow to collect the required integrated luminosity in a 5-year 10 TeV run, leaving also a spot both for a lower energy stage of $1\text{-}2 \text{ ab}^{-1}$ at 3 TeV and for a further increase of E_{cm} in the future. In Chapters 4 and 5 of this work, only the first 3 TeV stage will be studied, for which an integrated luminosity of 1 ab^{-1} will be assumed.

¹The size of the collider ring is currently limited by the field strength of the available bending dipole magnets.

Chapter 3

Experimental apparatus and event reconstruction

When running a high-energy physics experiment at a particle collider, it is essential to detect and reconstruct as accurately as possible the products of the hard scattering. The characteristics of both the detector and the algorithms employed must be suited for the environment in which the collisions happen.

In this chapter, the $\mu^+\mu^-$ collision environment is first described: the experimental apparatus and the technologies employed for the subdetectors, the characterisation of the beam-induced background (BIB) and the strategies to mitigate its effect in the detector. Finally, an overview of the software and the algorithms employed for the event simulation and physics objects reconstruction are described.

In this work, the following coordinates are used: the origin is set at the IP, the z axis is directed along the beam, the y axis is parallel with gravity and the x axis is orthogonal to the other two; the R axis is an arbitrary axis orthogonal with respect to z ¹.

3.1 Collision environment

3.1.1 The Detector

Given the breadth of Muon Collider physics program, a multi-purpose detector with an angular coverage close to 4π is required. The baseline for the Muon Collider Detector (MCD) design is the CLICdet concept [37], with a few modifications to fit the unique environment given by the presence of the beam-induced background, which generates a large particle flux that interacts with the detectors element.

¹the detector is symmetrical under rotations in the xy plane

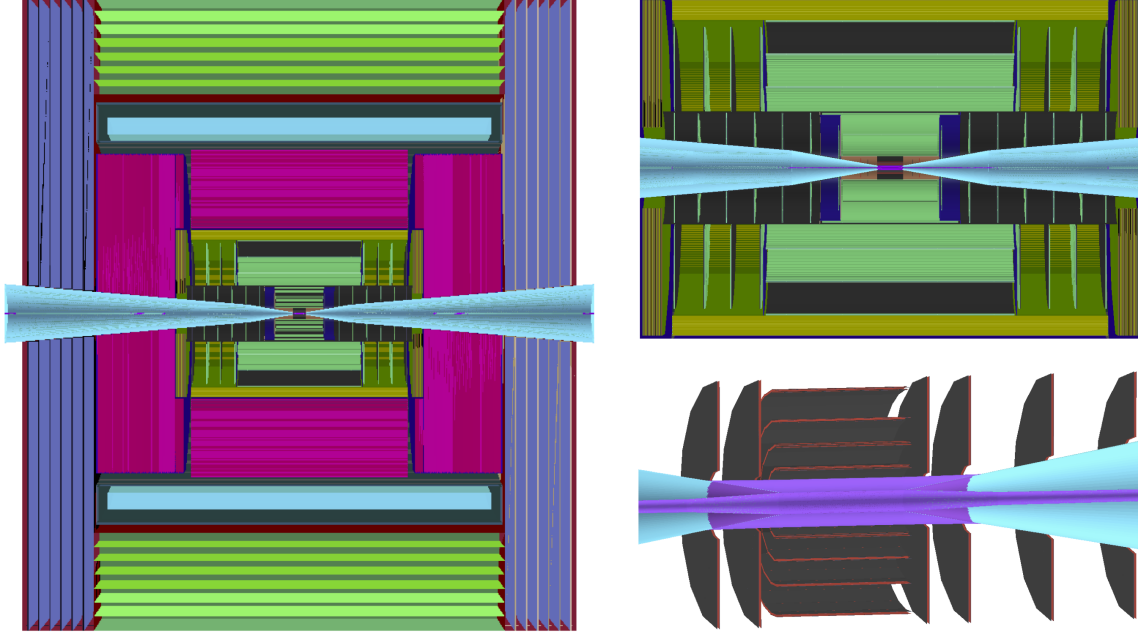


Figure 3.1: Sketch of the muon collider geometry used for the simulation studies. Shown are the cross sections of the full detector geometry (left) and two zoomed-in portions: up to ECAL (top right) and up to Vertex Detector (bottom right). The muon detectors (violet for the endcap, green for the barrel) surrounds the solenoid (cyan), which encloses the HCAL (magenta), ECAL (dark yellow) and the Tracking Detector (green and black). The shielding nozzles (cyan) and the beampipe (violet) are also shown. Taken from Ref. [38].

The overall detector, sketched in Figure 3.1, features a cylindrical layout around the beam pipe, with a radius of 6.45 m. The geometric parameters and the materials of the subdetectors are reported in Table 3.1.

Starting from the innermost subdetectors, the detection system is composed by:

- the tracking system, which includes a silicon vertex detector (VXD), an inner tracker (IT) and an outer tracker (OT);
- the calorimetry, consisting of a electromagnetic calorimeter (ECAL) and a hadronic calorimeter (HCAL);
- a superconducting solenoid, providing an inner magnetic field of 3.57 T;
- muon detection layers equipped with resistive plate chambers (RPC), interleaved within the magnet return yoke.

With respect to the CLICdet model, the most relevant changes introduced are in the tracker topology, made necessary by the introduction of two nozzles that enclose the beam

Subsystem	Region	R dimensions [cm]	Z dimensions [cm]	Material
Vertex Detector	Barrel	3.0 – 10.4	65.0	Si
	Endcap	2.5 – 11.2	8.0 – 28.2	Si
Inner Tracker	Barrel	12.7 – 55.4	48.2 – 69.2	Si
	Endcap	40.5 – 55.5	52.4 – 219.0	Si
Outer Tracker	Barrel	81.9 – 148.6	124.9	Si
	Endcap	61.8 – 143.0	131.0 – 219.0	Si
ECAL	Barrel	150.0 – 170.2	221.0	W + Si
	Endcap	31.0 – 170.0	230.7 – 250.9	W + Si
HCAL	Barrel	174.0 – 333.0	221.0	Fe + PS
	Endcap	307.0 – 324.6	235.4 – 412.9	Fe + PS
Solenoid	Barrel	348.3 – 429.0	412.9	Al
Muon Detector	Barrel	446.1 – 645.0	417.9	Fe + RPC
	Endcap	57.5 – 645.0	417.9 – 563.8	Fe + RPC

Table 3.1: Geometric parameters and materials of the muon collider subdetectors employed in the simulations presented in this paper. Taken from Ref. [38].

pipes. The introduction of these nozzles, consisting of double-cone shielding absorbers made of tungsten with a BCH_2 coating, was first proposed by the MAP collaboration [39] with the intent of shielding the tracker system and the calorimetry from the incoming flux of particles of the beam-induced background. The geometry and placement of the two nozzles, placed at an angle of 12° with respect to the beam axis and with a 12 cm distance between their tips, are optimized for a 1.5 TeV MuCol, for which a reduction of the BIB of three orders of magnitude can be achieved. Analyses [40] regarding BIB characterisation at 3 and 10 TeV are ongoing, and further studies are needed to investigate the optimization of the nozzles at those E_{cm} .

Tracking system

The tracking detectors allow both to reconstruct the trajectory of charged particles and to measure their momentum. In semiconductor detectors, a charged particle travelling through the tracker layers creates electron-hole pairs in the pixels (or strips), generating an electric signal that allows to reconstruct the "hits", and subsequently the track, of the particle. The presence of a magnetic field \vec{B} in the direction of the beam axis makes charged particles follow a helix-like trajectory. By reconstructing the radius of the trajectory r , the transverse momentum of the particle can be estimated as $p_{\text{T}} = q|\vec{B}|r$, where q is the charge of the particle (either negative or positive).

Each of the tracking subdetectors is composed of several layers arranged in two different regions: the barrel region, i.e. the central region, and the endcap region, i.e. the forward ($z > 0$) and backward ($z < 0$) region. The barrel layers are shaped as cylindrical surfaces, coaxial with the beam direction and centered in the IP. Endcap layers are instead annuli placed perpendicularly to the beam direction at the end of the barrel

layers, symmetrically for forward and backward regions. A sketch of the tracking systems of the MuCol detector is shown in Figure 3.2.

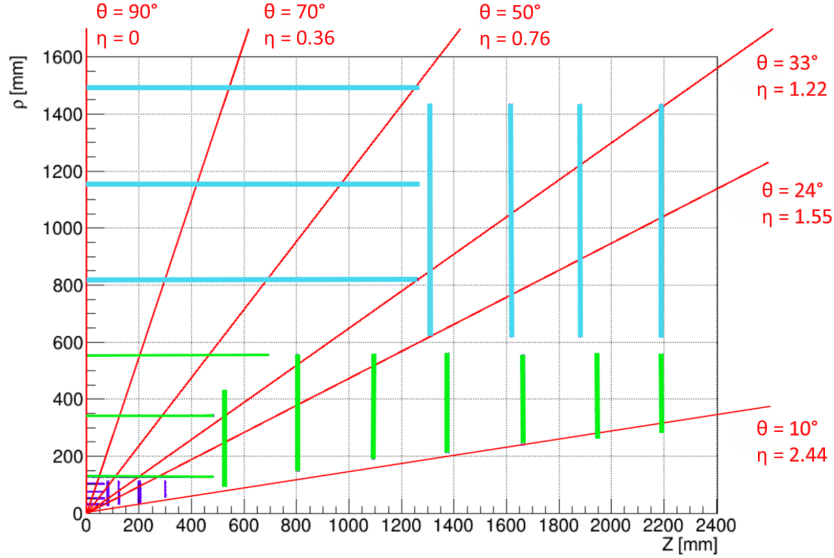


Figure 3.2: Sketch of the cross section of the tracker system of the muon collider detector in the $R - z$ plane: Vertex Detector (purple), Inner Tracker (green), Outer Tracker (cyan). The horizontal lines denote barrel layers, the vertical one the endcap modules. The double layered modules are not present in the picture. Only the first quadrant is shown, as other three are exactly symmetric. Taken from Ref. [41].

	Vertex Detector	Inner Tracker	Outer Tracker
Cell type	pixels	macropixels	microstrips
Cell Size	$25\ \mu\text{m} \times 25\ \mu\text{m}$	$50\ \mu\text{m} \times 1\ \text{mm}$	$50\ \mu\text{m} \times 10\ \text{mm}$
Sensor Thickness	$50\ \mu\text{m}$	$100\ \mu\text{m}$	$100\ \mu\text{m}$
Time Resolution	$30\ \text{ps}$	$60\ \text{ps}$	$60\ \text{ps}$
Spatial Resolution	$5\ \mu\text{m} \times 5\ \mu\text{m}$	$7\ \mu\text{m} \times 90\ \mu\text{m}$	$7\ \mu\text{m} \times 90\ \mu\text{m}$

Table 3.2: Type, size and resolution (temporal and spatial) of the VXD, IT and OT silicon layers. Taken from Ref. [38].

The tracking system follows the typical design of an all-Si tracker, and it is divided into three subdetectors: the Vertex Detector (VXD), the Inner Tracker (IT) and the Outer Tracker (OT), in order of proximity to the IP. Their characteristics and resolutions are reported in Table 3.2.

Each of the VXD modules is equipped with the double layer (DL) technology, i.e. it is composed of two layers of pixels, separated by a gap of 2 mm. These serve for the rejection of a large fraction of the BIB particles: the VXD is by far the subdetector with

the highest BIB occupancy²; the DL technology allows to identify the tracks with a large longitudinal displacement, a distinctive feature of BIB particles. This property can be used in the object reconstruction to improve the separation between the signal event and the BIB, as explained in Section 3.2.2.

Calorimetry

The calorimeter system is used to measure the energy of a particle by detecting the energy deposited in the calorimeter material in the form of electromagnetic or hadronic showers. Calorimeters are essential because they also work for neutral particles, which cannot be seen by the tracking system. The Muon Collider uses an electromagnetic calorimeter (ECAL) and an outermost hadronic calorimeter (HCAL), whose specifications are reported in Table 3.1.

In the current muon collider configuration, the sampling ECAL barrel and endcap modules are arranged in $5\text{ mm} \times 5\text{ mm}$ tiles, in which layers of tungsten absorber plates (1.9 mm thick) and Si pads sensors are alternated, corresponding to 22 radiation lengths X_0 (1 interaction length λ_I).

An alternative option for the ECAL, CRILIN [42] (CRystal calorImeter with Longitudinal Information), has been proposed and is currently under evaluation. CRILIN would feature semi-homogeneous calorimeter, in which Cherenkov light is emitted from particles passing through PbF_2 absorbers and is read out by SiPMs.

The sampling HCAL follows the same geometric structure of the ECAL. The barrel and the endcap modules are composed of $30\text{ mm} \times 30\text{ mm}$ cells, alternating steel absorber and plastic-scintillator tiles, corresponding to 7 interaction lengths λ_I .

Muon detectors

The muon detection layers are interleaved within the iron yoke used to return the magnetic field of the superconducting solenoid. They are used to identify muons and measure their momentum: any other particle coming from the IP stops in the other innermost subdetectors, while muons can penetrate and reach the muon detectors. To detect these particles, resistive plate chambers (RPC) divided into $30\text{ mm} \times 30\text{ mm}$ tiles are employed, which generate an electric signal every time a particle crosses them, allowing to identify the position of the hits. The barrel and endcap detectors are composed respectively of 7 and 6 layers.

²The occupancy is defined as the number of hits per unit of area.

3.1.2 BIB characterisation and mitigation strategies

The μ^- (μ^+) in the beams can decay in the beam pipe via the $\mu^- \rightarrow e^- \bar{\nu}_e \nu_\mu$ ($\mu^+ \rightarrow e^+ \nu_e \bar{\nu}_\mu$) process, generating a beam-induced background (BIB) of a high number of particles that can interact with the nozzles and the detector volume. To fully characterise the collision environment, it is essential to analyse the BIB properties and its effect in the experimental apparatus, which play a key role in the choice of the structure and the materials of the subdetectors.

BIB characterization

The BIB is simulated with a Monte Carlo multi-particle transport code, either MARS15 [43] or FLUKA [44, 45]. In this work, the results obtained with the latter are used. The particles produced in muon decays are propagated through the machine-detector interface (MDI). The BIB particles are then collected before entering the detector volume, and stored into files that may then be used to simulate their interactions with the detector. The results and plots regarding BIB characterisation shown in this section, unless otherwise specified, are obtained with simulated BIB coming from a 750 GeV μ^- beam³ (i.e. $\sqrt{s} = 1.5$ TeV), since the results are more complete and exhaustive, but one can find analogue distributions in the 3 and 10 TeV cases. As shown in Ref. [40], the MDI configuration and materials (especially the nozzles characteristics) play indeed the major role in determining the characteristics of the final state BIB particles. The optimization of the nozzles for a 3 and 10 TeV muon collider is therefore crucial, since it could significantly reduce the expected BIB levels at those center-of-mass energies.

The nozzles absorb the high energy particles produced by the muon decays and generate **electromagnetic showers**, **neutrons** and a minor contribution of **charged hadrons**. The BCH₂ cladding stops the slower neutrons, producing **photons**. A minimal amount of **Muons and antimuons** is generated via Bethe-Heitler pair production⁴.

The number of final state BIB particles after the MDI interaction, as given by FLUKA BIB simulations assuming a 1.5 TeV MuCol interaction region (IR) and MDI, are reported in Table 3.3 for a 0.75, 1.5 and 5 TeV muon beam. This huge flux of particles in the detector volume can make the $\mu^+ \mu^-$ signal event reconstruction challenging. The BIB particles occupancy in the tracker and calorimeters decreases rapidly as one moves away from the IP, therefore the VXD is the most exposed subdetector, while the HCAL is the least exposed one.

The BIB particles exiting the MDI are out-of-time (Figure 3.3a), soft (Figure 3.3b) particles, whose production vertex is longitudinally displaced from the IP. By employing high-resolution time-sensitive detectors, accounting for the BIB energy spectrum and de-

³The distributions of the BIB particles of a μ^+ beam would be mirrored, due to the symmetrical nature of the μ^- and μ^+ .

⁴The $\mu^+ \mu^-$ pair is produced from a photon emitted via Brehmsstrahlung by a (anti)muon in the beam pipe.

tecting the longitudinal displacement of the tracks, a large fraction of the beam-induced background may be suppressed, as presented in the next paragraphs.

Monte Carlo simulator	FLUKA	FLUKA	FLUKA
Beam energy [GeV]	750	1500	5000
μ decay length [m]	$46.7 \cdot 10^5$	$93.5 \cdot 10^5$	$311.7 \cdot 10^5$
μ decay/m/bunch	$4.3 \cdot 10^5$	$2.1 \cdot 10^5$	$0.64 \cdot 10^5$
Photons ($E_\gamma > 0.1$ MeV)	$51 \cdot 10^6$	$70 \cdot 10^6$	$107 \cdot 10^6$
Neutrons ($E_n > 1$ MeV)	$110 \cdot 10^6$	$91 \cdot 10^6$	$101 \cdot 10^6$
Electrons & positrons ($E_{e^\pm} > 0.1$ MeV)	$0.86 \cdot 10^6$	$1.1 \cdot 10^6$	$0.92 \cdot 10^6$
Charged hadrons ($E_{h^\pm} > 0.1$ MeV)	$0.017 \cdot 10^6$	$0.020 \cdot 10^6$	$0.044 \cdot 10^6$
Muons ($E_{\mu^\pm} > 0.1$ MeV)	$0.0031 \cdot 10^6$	$0.0033 \cdot 10^6$	$0.0048 \cdot 10^6$

Table 3.3: Number of BIB particles at the exit of the MDI (i.e. entering in the detector volume) as obtained from FLUKA simulations for different beam energies. The secondary BIB particles reported here are produced from the interactions of the muon decay products with the detector nozzles, and a minimum energy threshold was applied to ease the simulation process. Only the products of muons decaying within 100 m of the IP were considered. Taken from Ref. [28].

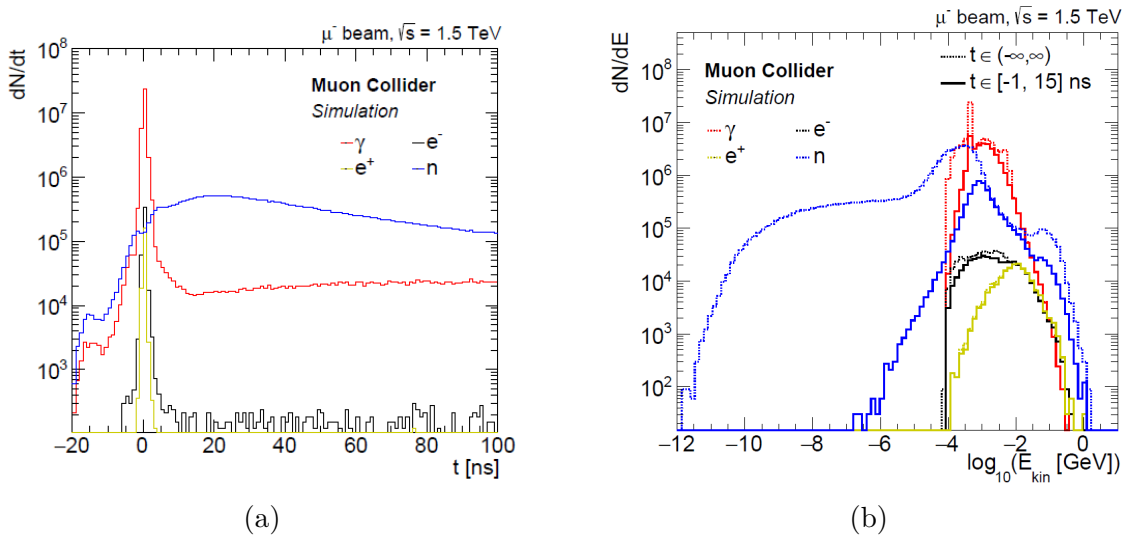


Figure 3.3: Distributions of time (a) and energy (b) of the main types of BIB particles exiting the MDI, with $t = 0$ being the bunch crossing time, as obtained from a 750 GeV beam simulated with FLUKA. Only the products of muons decaying within 100 m of the IP were considered. In the right plot, the effect of applying a time window around the bunch crossing time is also shown. Taken from Ref. [28].

BIB mitigation strategies

The strategies for reducing the BIB impact on the event reconstruction depend on the subdetector considered.

- **Tracking system:** the BIB hit occupancy is the highest here, especially in the Vertex Detector (up to 1000 hits/cm²). To reduce it and reject most of the "fake" BIB hits, a high granularity is needed, along with the DL filtering in the VXD (see Section 3.2.2), a high time resolution that allows the application of a very narrow acceptance time window, cluster shape analysis and the study of correlations between different tracker layers.
- **Calorimetry:** in these subdetectors, the BIB particles are mainly soft photons (96%) and neutrons (4%). A high cell granularity can reduce the probability of multiple particles depositing energy a single cell in the acceptance time window. A good time resolution (~ 100 ps) to reject the out-of-time BIB particles is also desirable, along with longitudinal segmentation (to perform cluster-shape discrimination) and a good energy resolution. The subtraction of part of the BIB energy deposits overlapping with the signal hits can be performed by a dedicated algorithm during the reconstruction step.
- **Muon detectors:** the BIB particles hit occupancy is low in the RPC layers, except for the very forward region, where high-energy neutrons and photons create hits near the MDI nozzles. A good granularity and energy resolution can help in performing a discrimination, together with lower cuts on the angle θ and on the reconstructed muons' momenta.

3.2 Physics objects reconstruction

In this section, the event simulation and the physics objects reconstruction workflow used in this thesis are discussed. The software used to simulate the events and the general workflow are presented, followed by a description of the different algorithms employed to reconstruct the physics objects in the MuCol framework.

3.2.1 Software and simulations

The software allows to perform detailed simulations of signal and BIB interactions with the complete detector, following the procedure used for example in Ref. [38]. The simulation is carried out with a MuCol forked version [46] of ILCSoftware [47], a framework specifically developed for the ILC which incorporates several key packages: DD4hep [48], which provides tools for describing detector geometry and interfaces for particle interaction handling; GEANT4 [49, 50, 51], which simulates particle interactions

as they pass through the passive detector material; the MARLIN [52] software environment.

The first step is the generation of the event, done with external programs such as Mad-Graph5 [53] or Python scripts. Meanwhile, BIB particles are generated through a combination of FLUKA [44, 45] and FLUKA LineBuilder [54], which calculate all products from beam-MDI interactions within 25 m of the IP, except for Bethe-Heitler muons, which are considered up to 100 m from the IP. Given the high BIB multiplicity, some strategies are employed to save RAM and CPU time: particles entering the MDI more than 25 ns after (and more than 1 ns before) the bunch crossing time are discarded; detector responses for very soft particles are not simulated; for relatively soft neutrons, a simplified, less CPU-intensive interaction model is used.

The energy deposited in the passive detector components is simulated separately for the signal and the BIB using GEANT4, producing simulated hits (SimHit collection). The response of each sensitive detector to the corresponding energy deposits returned by GEANT4 is then simulated by dedicated digitization modules implemented as MARLIN processors. During this phase, BIB and signal simulated hits are overlayed, producing the overall digitised response.

The tracking detector applies a Gaussian smearing to account for the spatial and time resolutions of local hit coordinates on the sensor surface and the time coordinate. The assumed resolution values are listed in Table 3.2. Acceptance time intervals, individually configured for each sub-detector, are used for replicating the finite readout time windows in the electronics of a real detector and to reject hits from asynchronous BIB particles. The output TrackerHit collection contains the ID of the pixel or microstrip where the hit was recorded, the timing information and the energy collected. The result of this simplified approach is one-to-one correspondence between the GEANT4 hits and digitized hits, which ignores the effect of charge distribution across larger area due to the Lorentz drift and shallow crossing angles with respect to the sensor surface.

The ECAL and HCAL detectors are digitized using realistic segmentation of sensitive layers into cells by summing all energy deposits in a single cell over a specific integration time. The time of the earliest energy deposit is assigned to the whole digitized hit. In the output CalorimeterHit collection, the ID of the cell is saved, as well as the total energy collected and the signal arrival time. The same digitization approach is used also for the muon detectors.

From the reconstructed hits, physics objects such as tracks and calorimeter clusters are reconstructed. Finally, the information from the different subdetectors is combined by particle flow algorithms to produce reconstructed particles, which are then subjected to higher-level analysis using external tools.

In this work, the version 2.8 (patch 2) of the Muon Collider Software, whose environment is available at [46], was used. Any modification to the default parameters is specified

in the text. Furthermore, the beamspot smearing has consistently been kept disabled during all the simulations. Its effects will be studied once the full digitization algorithm becomes operational.

3.2.2 Track reconstruction

In the magnetic field of the muon collider detector, a charged particle follows a helix trajectory aligned with the z axis. Deviations from a perfect helix can occur due to multiple-scattering, ionizing energy losses and bremsstrahlung. The charged particle trajectory is reconstructed from hits positions in the silicon tracking detector. The reconstructed object is called a track. A track consists of a set of hits (one per layer) and five fitted parameters describing the helix, listed in Table 3.4. A track reconstruction algorithm can roughly be broken up into two steps: pattern recognition to identify the hits belonging to a single track and fitting the hit coordinates with a track model to deduce the relevant track parameters.

Parameter	Definition	Description
d_0	$y_0 \cos \phi - x_0 \sin \phi$	Signed transverse impact parameter [mm]
z_0	z_0	Longitudinal impact parameter [mm]
$\tan \lambda$	p_z/p_T	Tangent of the angle between the helix and the xy plane
Ω	$c \vec{B} q/p_T$	Signed curvature of the track [mm^{-1}]
ϕ	$\arctan(p_y/p_x)$	Angle in the xy plane at (x_0, y_0, z_0) [rad]

Table 3.4: The five parameters used in the MARLIN software to parametrize the tracks, with the relative definitions and default units of measurement. ϕ refers to the azimuthal angle, q to the charge of the particle, c to the speed of light, x_0, y_0, z_0 to the x, y, z coordinate of the track trajectory point closest to the IP.

Two tracking algorithms are discussed in this thesis: the Conformal Tracking and the Combinatorial Kalman Filter.

Conformal Tracking

The Conformal Tracking (CT) algorithm [55] was originally developed to work in the clean environment of e^+e^- colliders. As such, its use is currently unfeasible in the MuCol environment, where the presence of the BIB makes the time required to run the algorithm prohibitive, even in presence of strategies to mitigate the problem. Nevertheless, the CT remains a precious tool to test the tracks and physics objects reconstruction at the MuCol in the absence of BIB with a well-established algorithm. It is embedded in the MARLIN

software.

The CT uses the conformal mapping technique [56], which transforms the coordinates in the transverse plane (x, y) in a new set of coordinates (u, v) , for which the equation of motion of the charged particle follows a straight line. To account for deviations of the trajectory due to e.g. multiple scattering or non-prompt particles, the pattern recognition in the (u, v) coordinates is performed with the cellular automaton technique [57]. More details are available in Ref. [55].

Combinatorial Kalman Filter

The Combinatorial Kalman Filter (CKF) algorithm, which exploits the Kalman formalism [58], is implemented using the A Common Tracking Software (ACTS) library [59], an experiment-independent open-source software toolkit available as a MARLIN processor. The ACTS code is optimized for parallel execution and vectorization, which makes it efficient and fast. This makes it perfectly suited to deal with the large hit multiplicity generated by the BIB.

The reconstruction of a charged particle track in ACTS, which requires as inputs the tracker geometry and materials and the digitised hits collection, proceeds through the following steps:

1. **Clustering** of the hits in the tracker detector;
2. **Space point formation** in the 3-D space;
3. **Seeding** using triplets of space points which are likely to come from the same track;
4. **Track finding with CKF** to search for hits generated by the same particle in the other tracker layers, starting from the seeds;
5. **Track fitting** to extract the track parameters;
6. **Vertex finding and fitting** to reconstruct the production vertex (primary or secondary) of the charged particle(s).

Tracks are finally refitted again, possibly adding cuts on the number of hits in each subdetector and on the χ^2 of the track.

For both the CT and the ACTS tracking algorithm, the double layer (DL) filtering can be enabled to increase the BIB discrimination. This is done by requiring the two hits in the tracker DL modules to be compatible (within a certain margin) with the trajectory of a particle coming from the IP. This allows a large reduction of the BIB-induced tracks, with a magnitude depending on the working point of the DL filtering algorithm.

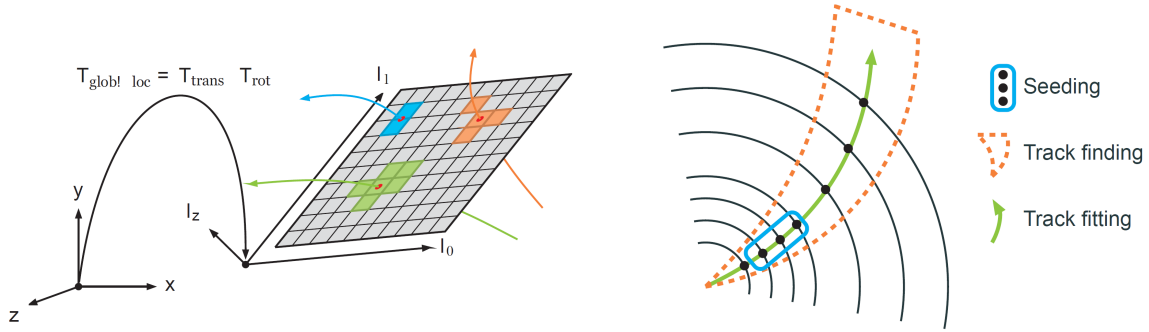


Figure 3.4: Some steps of the tracking algorithm that leads to the track reconstruction: the spacepoint formation (left), which entails a transformation of the coordinate system to adapt to the tracker one; the seeding, track finding (i.e. the action of the Kalman filter) and track fitting (right). Taken from Ref. [60].

3.2.3 PandoraPFA

The Pandora Particle Flow Algorithm [61] (PandoraPFA) is responsible for the reconstruction of the physics objects using inputs from the different subdetectors, such as tracks, ECAL and HCAL energy deposits and muon detectors hits. The particle flow approach to calorimetry is meant to improve the jet energy resolution by tracing the paths of individual particles through the detector, gathering the energy deposits left in each subdetector system. The energy and momentum for each particle can then be extracted from the subdetector system in which the measurement is expected to be most accurate: the tracker for charged particles momenta, the ECAL for photon energies, the HCAL for the long-lived neutral hadrons.

PandoraPFA uses more than 60 different algorithms, which details can be found in Ref. [62, 63]. The basic reconstruction operations performed by these algorithms can be summarised as follows:

1. Calorimeter cells are clustered using a simple cone-based clustering algorithm, working outwards: from the front of the ECAL to the back of the HCAL. Clusters can be seeded by projecting the tracks to the front of the ECAL;
2. The clustering algorithm is configured so that it tends to split up the energy deposits from individual particles, rather than merging merging energy deposits of different particles. Topological clustering algorithms are then used to merge the resulting proto-clusters;
3. The calorimeter clusters are matched to the inner detector tracks by comparing the properties of the clusters with the projected track states at the front ECAL, employing also linear and helix fits;

4. Statistical reclustering is applied to calorimeter clusters not in agreement with the associated track momentum: series of clustering algorithms are used to find the best track-cluster compatibility;
5. Fragment-removal algorithms look for neutral clusters (without track association) that may be fragments of nearby charged clusters (with track associations) by evaluating the changes in track-cluster compatibility that would occur if the clusters were merged;
6. Particle flow objects (PFOs) are constructed by combining tracks and associated clusters. For particles containing both, properties are primarily extracted from the tracks. In the case of neutral particles, calorimeter data is utilized to determine their characteristics;
7. Dedicated algorithms assign Particle Data Group (PDG) codes to the reconstructed particles, effectively identifying charged leptons. While photon identification is considered throughout the whole reconstruction process, it is finalized at this stage.

The output particle flow objects (PFOs) may be used for the higher level data analysis and processing with other MARLIN processors to perform physics studies, such as the TAU-FINDER algorithm for τ leptons reconstruction, described in Chapter 4.

Chapter 4

Tau lepton reconstruction and identification

The tau (τ) lepton, its properties and its reconstruction techniques play a crucial role in studying the $H \rightarrow \tau\tau$ process at the Muon Collider (MuCol). τ leptons are reconstructed from their decay products using a dedicated algorithm. In the MARLIN software for the Muon Collider event reconstruction, the algorithm used for this task is TAUFinder. In this study, the version 2.8 (patch 2) of the Muon Collider software environment [46] was used.

In this chapter, the performance of TAUFinder at a 3 TeV MuCol is evaluated. First, a description of the basic properties of the τ lepton is provided. Then, a study of the charged pions reconstruction efficiencies at a 3 TeV MuCol is presented, which is preparatory for the τ_h reconstruction. After a description of the algorithm, the results on the τ_h identification efficiencies are reported. The final sections are dedicated to the τ misidentification and to the computation of the τ energy corrections.

Given the numerous challenges related to its implementation in the software and computational time required, the BIB was not directly included in the analysis, and the Double Layer filtering algorithm was turned off. Nevertheless, the presence of an acceptance window for the particles' arrival time (discussed in Section 3.2.1) in each of the subdetectors, together with the high ECAL energy threshold, allow to indirectly, even if only partially, account for the effect of the soft, out-of-time BIB particles.

4.1 The tau lepton in the Standard Model

The τ^- lepton is an elementary particle of the SM. It is a fermion belonging to the third generation, with electric charge -1, spin 1/2 and weak isospin -1/2. As it is a lepton, it has no color charge and it is not involved in strong interactions. It has a mass $m_\tau = 1.777 \text{ GeV}/c^2$, and a quantum number conjugate antiparticle, the τ^+ .

In the SM, the τ^- (τ^+) lepton can be produced e.g. as the decay product of bosons, in the $H \rightarrow \tau^+\tau^-$, $Z/\gamma^* \rightarrow \tau^+\tau^-$ and $W^\pm \rightarrow \tau^\pm\nu_\tau$ processes, or in the charged current interaction of a tauonic (anti)neutrino ν_τ ($\bar{\nu}_\tau$) with another particle, $\nu_\tau X \rightarrow \tau^- X'$ ($\bar{\nu}_\tau X \rightarrow \tau^+ X'$). The SM Lagrangian terms describing the charged current (CC) and neutral current (NC) weak interactions of the τ^- are the following:

$$\mathcal{L}_{\text{CC}}^{(\tau)} = -\frac{g}{\sqrt{2}} \left[\bar{\tau}_L \gamma^\mu \nu_{\tau L} W_\mu^- + \bar{\nu}_{\tau L} \gamma^\mu \tau_L W_\mu^+ \right], \quad (4.1)$$

$$\mathcal{L}_{\text{NC}}^{(\tau)} = -\frac{g}{\cos \theta_W} \left[\left(-\frac{1}{2} + \sin^2 \theta_W \right) \bar{\tau}_L \gamma^\mu \tau_L + \sin^2 \theta_W \bar{\tau}_R \gamma^\mu \tau_R \right] Z_\mu. \quad (4.2)$$

Once produced, the τ^- lepton is unstable, with a mean lifetime of 2.9×10^{-13} s [5]. It decays via the weak interaction into a ν_τ and a W^- boson (see Equation 4.1). Analogously, the τ^+ decays into a $\bar{\nu}_\tau$ and a W^+ boson. Subsequently, the W boson decays either into a $\ell\nu_\ell$ pair (charged lepton and a neutrino) or a $q\bar{q}'$ pair (up-type quark and down-type quark), as shown in Figure 4.1. τ leptons decaying leptonically are denoted as τ_ℓ , while τ leptons decaying hadronically are denoted as τ_h .

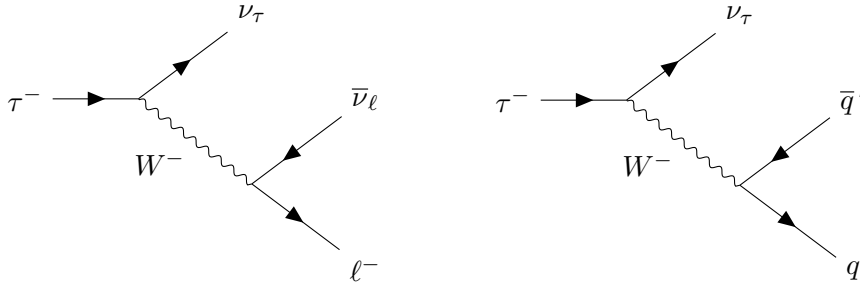


Figure 4.1: Feynman diagrams for a τ^- lepton decaying into leptonic (left) and hadronic (right) final states.

For a τ_h , the final state particles after the hadronization are light charged and neutral mesons, mainly π^\pm , K^\pm and π^0 . The main τ SM decay modes are reported in Table 4.1. Since the τ lepton has a $Q = \pm 1$ electric charge, the final states of a τ_h can include either one or three charged hadrons (h^\pm); this is used to classify the hadronic decay modes in 1-prong (one h^\pm , $\approx 50\%$ of the total τ decays) and 3-prong (three h^\pm , $\approx 15\%$ of the total τ decays).

4.2 Tau leptons at high energy colliders

The first evidence for the existence of τ lepton was found in 1975 at SPEAR [65], a 4.8 GeV e^+e^- collider hosted at SLAC. Since then, many collider (such as LEP [66]) have performed in-depth studies of the τ properties, such as its mass, its lifetime, its CC

Decay mode	Resonance	\mathcal{B} (%)
Leptonic decays		35.2
$\tau^- \rightarrow e^- \bar{\nu}_e \nu_\tau$		17.8
$\tau^- \rightarrow \mu^- \bar{\nu}_\mu \nu_\tau$		17.4
Hadronic decays		64.8
$\tau^- \rightarrow h^- \nu_\tau$		11.5
$\tau^- \rightarrow h^- \pi^0 \nu_\tau$	$\rho(770)$	25.9
$\tau^- \rightarrow h^- \pi^0 \pi^0 \nu_\tau$	$a_1(1260)$	9.5
$\tau^- \rightarrow h^- h^+ h^- \nu_\tau$	$a_1(1260)$	9.8
$\tau^- \rightarrow h^- h^+ h^- \pi^0 \nu_\tau$		4.8
Other		3.3

Table 4.1: Decays of τ leptons and their branching fractions in percentage [64]. For the decay modes with intermediate resonances, these are shown in the middle column. Charged hadrons are denoted by the symbol h^\pm . Only τ^- decays are shown, since the decays and values of the branching fractions are identical for charge-conjugate decays.

and NC interactions and its branching fractions, to verify their agreement with the SM predictions.

For an unstable particle, the decay length is defined as the distance travelled by a particle at which the probability for it to have decayed is equal to $1/e$. If the particle is ultrarelativistic ($v \approx c$), the decay length is equal to $\gamma\beta c\tau$, where γ is the Lorentz factor, τ is the mean lifetime of the particle and $\beta = v/c$, where c is the speed of the light in the vacuum. For τ leptons, $c\tau_\tau \approx 87 \mu\text{m}$. Considering a τ with an energy of 10 GeV in the laboratory frame, the resulting decay length is $\gamma\beta c\tau_\tau \approx 0.5 \text{ mm}$, while for a 100 GeV τ , $\gamma\beta c\tau_\tau \approx 5 \text{ mm}$. This distance needs to be compared with the distance of the ATLAS and CMS inner trackers from the interaction point, that is equal respectively to 3.3 cm [67] and 2.9 cm [68]. This means that the τ lepton cannot be detected directly, but only through the interaction of its decay products, charged leptons and hadrons, with the detector.

It is crucial to remark that the ν_τ neutrino produced in the decay, given its small cross section of interaction with the detector elements, is not detected. Nevertheless, the fact that in such colliders the initial transverse momentum of the p-p system is null can be exploited. Indeed, it is possible to compute the missing transverse momentum vector \vec{p}_T^{miss} as the negative vector sum of the transverse momenta of all the particle flow objects in an event (applying the necessary energy corrections). This can be used to estimate the transverse momentum carried by the neutrino(s) produced in the event.

Once the τ decay products in a p-p collision have been reconstructed and identified, a reconstruction algorithm is run to reconstruct the τ_h candidates from the final state

hadrons. Then, a τ identification (ID) algorithm can be run on the τ_h s candidates to test whether the reconstructed tracks and hadronic objects of the event, and possibly the value of $|\vec{p}_T^{\text{miss}}|$, were actually produced in a τ_h decay or not. Jets from τ_h decays have generally less energy in their surroundings (i.e. have more isolation) than genuine hadronic jets, which make up for most of the background, and this allows to build powerful discrimination variables between the two. Instead, the separation between prompt charged leptons and charged leptons coming from τ_ℓ decays can only be performed by a study of the distribution of the impact parameter d_0 (see Section 3.2.2).

After these tests, checks and cuts, if the τ candidate passes the selection it is tagged as a τ_h (or τ_ℓ), i.e. identified as a τ lepton. By way of example, the algorithms employed for τ reconstruction and identification by the CMS experiment are described in Appendix A.

4.3 Charged pion reconstruction

As introduced in Section 4.1, a significant fraction ($\approx 65\%$) of τ leptons decays into charged hadrons, either via 1-prong ($\approx 50\%$) or 3-prong ($\approx 15\%$) decays. To accurately reconstruct the τ_h , it is crucial to properly reconstruct the charged hadrons resulting from its decay. Therefore, the initial focus must be on studying the reconstruction efficiencies of the charged hadrons, particularly pions.

An important tool for this study are simulations of "particle guns", i.e. events with a single particle that is generated and propagated from the interaction point outwards. The simulation of the interaction of the particle with the detector, the digitisation of the signal and the event reconstruction are then performed according to the workflow employed for the standard $\mu^+\mu^-$ collision events.

A sample of 200k particle gun events, consisting of 100k π^+ and 100k π^- , was generated with a Python script. The properties of the generated particle guns were randomly extracted from the following distributions:

- p_T - uniformly distributed in the [5 GeV, 300 GeV] interval;
- ϕ (azimuthal angle) - uniformly distributed in the $[-\pi, +\pi]$ interval;
- θ (polar angle) - uniformly distributed in the $[10^\circ, 170^\circ]$ interval¹.

The choice of $\theta \in [10^\circ, 170^\circ]$ is motivated by the fact that the tracker and the calorimetry are only installed in this range, given the presence of the nozzles (located at $\approx 12^\circ$ and 168°). The sample containing the generated particles was then fed into GEANT4 for simulating the interaction with the detector, and subsequently the digitisation and reconstruction MARLIN processors were run (see Section 3.2.1), using the Combinatorial Kalman Filter tracking algorithm. As stated at the beginning of this section, the BIB

¹A polar angle $\theta = 10^\circ$ (170°) corresponds to a pseudorapidity $\eta = 2.436$ (-2.436).

was not included in the workflow. The output of the reconstruction process is then analyzed with the LCTuple package [69], which produces a ROOT file with ROOT NTuples containing information regarding the Monte Carlo generated particles, the tracks, the reconstructed particles and other properties of the event. Comparing the information of the MC particle guns with the reconstructed tracks and Particle Flow (PF) objects, it is possible to compute the efficiencies.

First, an analysis of the tracking efficiency was performed. Since each event contains a single MC π^\pm , the track reconstruction efficiency is defined as

$$\epsilon_{\text{trk}} = \frac{\text{Number of events with a matched reconstructed track}}{\text{Total number of } \pi^\pm \text{ gun generated events}}. \quad (4.3)$$

The matching of the reconstructed charged track with the generated pion was done by requiring $\Delta R = \sqrt{(\Delta\eta)^2 + (\Delta\phi)^2} < 0.1$, where ΔR is the distance in the $\eta - \phi$ plane between the MC particle and the reconstructed track, with the track momentum components calculated at the IP. The efficiency was studied both as a function of the transverse momentum p_T^{gen} and of the pseudorapidity η^{gen} of the generated pion. An example of the distributions obtained is shown in Figure 4.2.

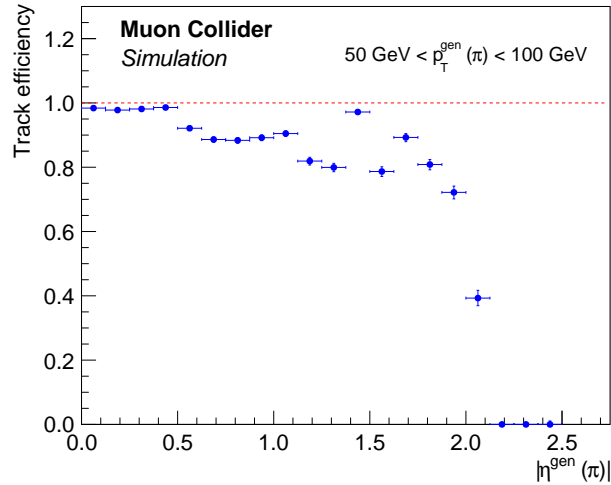


Figure 4.2: Pion tracking efficiency estimated with the Combinatorial Kalman Filter algorithm as a function of the pseudorapidity of the pion, in the $50 \text{ GeV} < p_T^{\text{gen}}(\pi) < 100 \text{ GeV}$ range. The π^\pm analyzed are part of the particle guns generated samples detailed in the text.

The discontinuities in the efficiencies that can be seen in Figure 4.2 for $|\eta| > 0.5$ were analyzed, and the cause was identified as an issue of the tracking algorithm: the Combinatorial Kalman Filter [58] implemented in A Common Tracking Software [59] (ACTS) is underestimating the error associated to the position of subsequent hits in the endcap

disks. The small uncertainty prevents the fit from converging, hence the track is discarded during the refitting stage. Further investigations of the issue are ongoing, together with improvements of the tracking system that would allow an enhanced performance of the physics studies.

The pion reconstruction efficiency was then studied, by comparing the generated pions with the reconstructed PF objects produced by PandoraPFA. The charged pion reconstruction efficiency is here defined as

$$\epsilon_{\pi} = \frac{\text{Number of events with a matched } \pi^{\pm}}{\text{Total number of } \pi^{\pm} \text{ gun generated events}} \quad (4.4)$$

The matching of the reconstructed charged pion with the generated pion was done by requiring both $\Delta R < 0.1$, where ΔR is the distance in the $\eta - \phi$ plane between the two pions, and $p_T^{reco} \in [0.9 \cdot p_T^{gen}, 1.1 \cdot p_T^{gen}]$, where p_T^{reco} is the reconstructed transverse momentum and p_T^{gen} is the transverse momentum of the generated pion. The distributions of ΔR and p_T^{reco} were studied as well, to ensure that the kinematic variables were similar in the reconstructed and in the generated pions.

The pion reconstruction efficiency was studied as a function of the pseudorapidity η^{gen} (Figure 4.3a) and of the transverse momentum p_T^{gen} (Figure 4.3b) of the generated pion. The results obtained show a poor reconstruction efficiency. The cause of this issue was found to be the high value of the energy activation thresholds of the ECAL and the HCAL calorimeter cells. The threshold values originally inherited from the CLIC experiment were 50 keV for the ECAL and 250 keV for the HCAL. Given the background noise caused by the presence of the BIB low-energy particles, absent in CLIC, the default MuCol software threshold values were increased to 2 MeV for both the ECAL and the HCAL as a "quick-and-dirty" solution to suppress the BIB, reducing the computational time required to process a single event.

Studies were then performed to improve the reconstruction efficiency. The solution found was to decrease the HCAL threshold from 2 MeV to 250 keV, bringing it back to its original CLIC value. This is also motivated by the fact that the HCAL has a lower BIB occupancy than the ECAL, since it is further away from the IP. The reconstruction of the events was executed again, with the new value of the HCAL threshold. The reconstruction efficiencies of the π^{\pm} obtained for the two different HCAL energy thresholds are shown as a function of $|\eta|$ (Figure 4.3a) and p_T (Figure 4.3b).

The π^{\pm} reconstruction efficiency obtained with the new HCAL threshold (250 keV) is compared in Figure 4.4 with the tracking efficiency reported in Figure 4.2. The ratio of the two plotted as a function of the pseudorapidity displays some anomalies: a drop around $|\eta| = 1$, a recovery around $|\eta| = 1.4$ and then another drop. This behavior was found to be due to the PandoraPFA algorithm (see Section 3.2): in some cases, the track is reconstructed but is not correctly associated with the cluster, leading to the reconstruction of neutrons (i.e. HCAL clusters without an associated track) instead of

charged pions. An attempt was made to find a solution to the problem, such as loosening the requirements on the track-cluster distance, but no satisfactory results were achieved. The issue is still under investigation by the MuCol community.

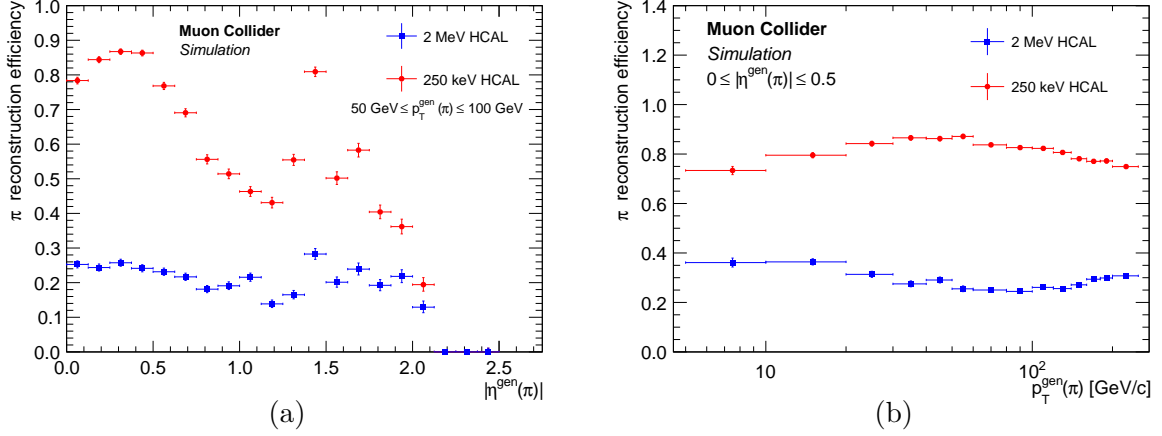


Figure 4.3: Charged pion reconstruction efficiencies as a function of the pseudorapidity (a) and transverse momentum (b) of the generated charged pions, shown for the p_T^{gen} and $|\eta^{\text{gen}}|$ ranges reported in the figures. The efficiencies are reported for two different HCAL energy thresholds: the MuCol default one of 2 MeV (in blue) and the 250 keV one (in red) used in this study. The π^\pm analyzed are part of the particle guns sample detailed in the text.

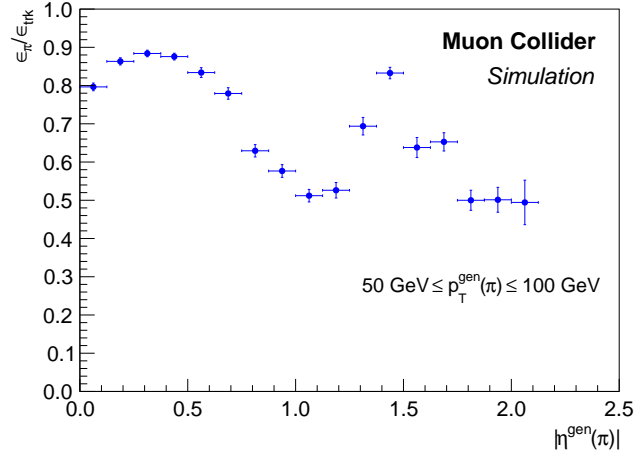


Figure 4.4: Ratio between the estimated π^\pm reconstruction efficiency (defined in Eq. 4.4) and the estimated π^\pm tracking efficiency (as defined in Eq. 4.3), shown as a function of the generated π^\pm pseudorapidity, in the $50 \text{ GeV} \leq p_T^{\text{gen}} \leq 100 \text{ GeV}$ range. The efficiencies reported were obtained from a 200k π^\pm particle guns sample, as detailed in the text.

4.4 Tau lepton reconstruction

The TAUFINDER algorithm [70] is the MuCol software algorithm designed to reconstruct τ leptons from their decay products. In this section, a description of the algorithm is provided, and the studies carried out to characterise its performance are discussed.

4.4.1 The TauFinder algorithm

TAUFINDER [70] was developed in the framework of the e^+e^- CLIC experiment, hence it is designed for τ reconstruction at lepton colliders. It resembles a jet-finding cone algorithm, using the four-momentum vectors of all detectable charged and neutral particles. The key steps are:

1. Seeding: The algorithm begins by testing the charged particles as potential seeds for τ candidates, starting from the particle with the highest energy;
2. Cone formation and jet reconstruction: once a seed is identified, the algorithm defines a search cone with an opening angle of 0.05 in the $\eta - \phi$ space around it. The charged particles within this cone are added to the τ candidate one at a time, and every time the cone axis is dynamically adjusted to the particles' combined momentum. Following this, neutral particles within the search cone are also added in the same fashion;
3. Steps 1) and 2) are iteratively repeated, until no charged particle in the event is left out;
4. Reconstruction and Merging: After all potential τ candidates are identified, their momenta and energies are combined to form reconstructed τ leptons. A final check is performed to merge any candidates that were mistakenly split, ensuring a more accurate reconstruction.

The selection of τ candidates involves a series of cuts, which ensure that only the most likely candidates are accepted, while reducing the risk of false positives and background contamination.

The **fixed quality cuts**, which are not customisable, are the following:

- Charged particles multiplicity: Since τ decays can be either 1-prong or 3-prong, the number of reconstructed charged particles allowed within the search cone is restricted between one and three;
- Particle count: The total number of particles (charged and neutral) associated with a τ candidate is restricted to be fewer than ten;

- Charge: The charge of the reconstructed τ candidate must sum to either +1 or -1, consistent with the value of the τ lepton charge.

The **reconstruction and isolation cuts** consist of:

- Minimum p_T : A cut is applied to suppress background by requiring a minimum p_T of 1 GeV/c for any reconstructed object to be considered in the algorithm. Additionally, the τ seed itself must have a minimum p_T of 5 GeV/c, to ensure that only a significant reconstructed charged particle initiates the reconstruction process;
- Isolation energy: An isolation cone is drawn in the $\eta - \phi$ plane around the signal cone, with an additional opening angle of 0.2 rad, to evaluate the energy in the τ candidate surroundings. An upper limit of 5 GeV is set on the sum of the energies of reconstructed particles within the isolation cone, to help the discrimination against genuine hadronic jets.

The reconstruction and isolation cuts values, as well as the search and isolation cones opening angles, can be customised. This allows to tailor the algorithm for specific datasets or experimental setups, optimizing the balance between identification efficiency and background rejection. For example, in environments with higher background noise, the transverse momentum cuts can be raised to reduce false positives, or the isolation criteria can be tightened to ensure greater purity in the τ sample. In this first study of TAUFinder at a muon collider, these user-defined parameters were kept at their default values.

The candidates passing all the selection are declared as reconstructed τ^+ or τ^- leptons, based on their charge (+1 or -1).

4.4.2 TauFinder performance

To assess the τ leptons reconstruction performance of TAUFinder, a sample of 200k particle gun events of 100k τ^+ and 100k τ^- was generated, with:

- p_T - uniformly distributed in the [5 GeV, 800 GeV] interval;
- ϕ (azimuthal angle) - uniformly distributed in the $[-\pi, +\pi]$ interval;
- θ (polar angle) - uniformly distributed in the $[10^\circ, 170^\circ]$ interval.

The workflow of the simulation is analogous to what was done for the charged pion guns, except that the τ is unstable. During the generation of the τ particle gun in the Python script, the kinematical properties are assigned to the τ , and the coordinates at which

it decays are computed; then GEANT4, in the simulation of the interaction with the detector, takes care of the τ decay process.

It is important to remark that the Muon Collider software is not yet provided with an algorithm to reconstruct the missing transverse momentum carried away by the ν_τ in the τ decay process. Hence, it is only possible to reconstruct the visible decay products (leptons, hadrons, etc.), while the original momentum of the τ is currently not accessible.

The first thing to observe is that TAUFinder does not discriminate between τ leptons decaying hadronically (τ_h) and leptonically (τ_ℓ); a selection of the reconstructed τ_h can be performed by requiring the presence a charged hadron (or a charged lepton) amongst the particles combined to form the τ candidate. Moreover, the Muon Collider detector and software are not provided with a π^0 reconstruction system. Hence, in the τ_h decays producing one or more neutral pions, only photons are reconstructed as final state particles; the classification of the reconstructed τ_h decay modes was done solely on the basis of the number of prongs (i.e. charged pions combined to form the τ candidate).

Since this analysis focuses on the hadronically decaying taus, only the events with the generated τ decaying hadronically were selected to study the efficiency. Amongst these events, the τ_h reconstruction efficiency can be defined analogously to the π^\pm reconstruction efficiency as:

$$\epsilon_\tau = \frac{\text{Number of events with one matched } \tau_h^\pm}{\text{Total number of } \tau_h^\pm \text{ generated events}}. \quad (4.5)$$

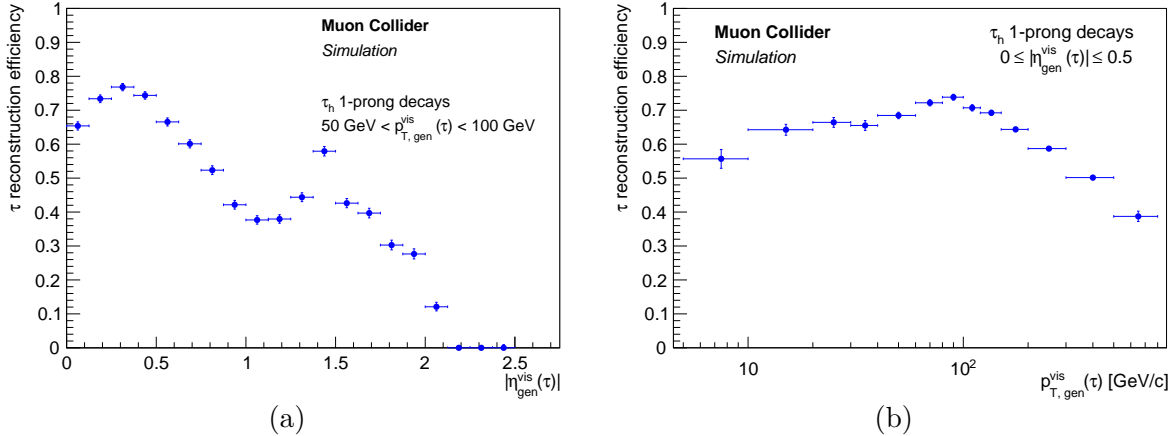


Figure 4.5: 1-prong τ_h leptons reconstruction efficiencies obtained with the TAUFinder algorithm, as a function of the pseudorapidity (a) and the transverse momentum (b) of the system formed by the generated visible products of the τ_h 1-prong decays, shown for the p_T^{gen} and $|\eta^{\text{gen}}|$ ranges reported in the figures. The τ leptons analyzed are part of the τ particle guns sample detailed in the text.

The matching was done by requiring $\Delta R < 0.1$, where ΔR is the distance in the $\eta - \phi$ plane between the visible products of the generated τ_h and the reconstructed τ_h .

In Figure 4.5, the τ_h identification efficiency is shown as a function of the pseudorapidity (left) and transverse momentum (right) of the generated τ_h .

To further investigate the drop in efficiency, the ratio of the 1-prong τ_h efficiency and the π^\pm reconstruction efficiencies is shown in Figure 4.6. The ratio is approximately constant up to $|\eta| \lesssim 1$, with a slight shift downwards due to the TAUFINDER cuts and to the lower efficiency in the $\pi^\pm + \pi^0$ s decay channels. For $|\eta| > 1$, the ratio tends to decrease showing some spikes and drops, whose nature is yet to be identified and is currently under investigation.

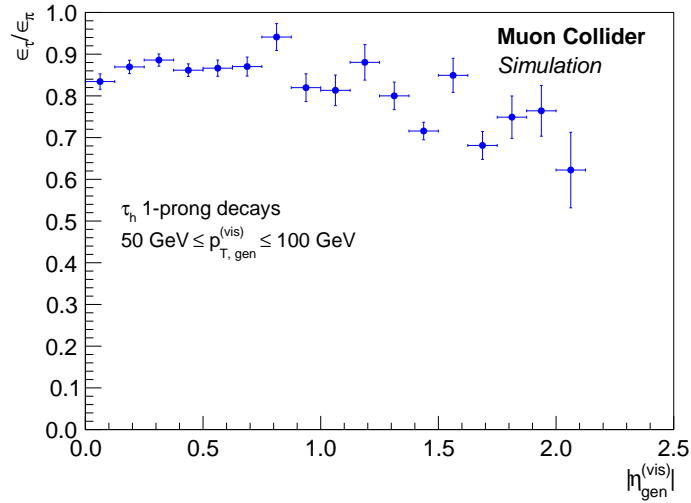


Figure 4.6: Ratio between the estimated 1-prong τ_h reconstruction efficiency (defined in Eq. 4.5 and shown in Figure 4.5) and the estimated π^\pm reconstruction efficiency (defined in Eq. 4.4 and shown in Figure 4.3), shown as a function of the generated pseudorapidity of the π^\pm or of the visible decay products of the τ_h , in the $50 \text{ GeV} \leq p_{T,gen}^{(vis)} \leq 100 \text{ GeV}$ range. The efficiencies reported were obtained from a 200k τ^\pm and a 200k π^\pm particle guns samples and in the 250 keV HCAL configuration (see text).

4.4.3 Tau misidentification

In the context of τ lepton reconstruction and identification, a crucial role is played by misidentification, i.e. events in which a physics object that is not a τ , for example a genuine hadronic jet or an electron, is reconstructed and identified as a τ . These misidentified objects are also called "fake" τ s. In this work, of particular interest is the misidentification as fake τ_h , i.e. physics objects reconstructed by TAUFINDER as

hadronically decaying τ s. A low misidentification rate is essential when performing high-precision measurements of processes such as the $H \rightarrow \tau\tau$ decay, investigated in Chapter 5, to avoid the contamination of events with one or more fake τ_h s in the final state.

To quantify the TAUFinder τ_h misidentification rates of light-flavored jets², electrons and b -jets, samples of $\mu^+\mu^- \rightarrow Z\nu_\mu\bar{\nu}_\mu$, $Z \rightarrow X$ events were generated with MadGraph5. Specifically, the three samples generated consist of: 100k $Z \rightarrow jj$ events (a Z decaying into two light-flavored jets), 100k $Z \rightarrow b\bar{b}$ events, 100k $Z \rightarrow e^+e^-$ events. In each of these samples, the generated jets/electrons were required to have $|\eta| < 2$ and $20 \text{ GeV}/c \leq p_T \leq 300 \text{ GeV}/c$. The misidentification rate was obtained by simply dividing the total number of reconstructed τ_h s in the sample by the total number of generated jets/electrons in the sample. Table 4.2 shows the misidentification rates obtained with this procedure.

Physics object	Misidentification rate
Light-flavored jets (u, d, s)	5.8%
b -jets	3.9%
Electrons	2.8%

Table 4.2: Misidentification rates of various physics objects as τ_h . The rates are integrated over the full samples.

It is interesting to observe that the misidentification of a prompt electron as τ_h can occur only when the electron is misidentified as a charged hadron by PandoraPFA, since TAUFinder only performs a merging of the output PF objects.

Other than the amount of energy deposited in the isolation cone, already used by TAUFinder to reject genuine hadronic jets, a key variable to distinguish real τ s from jets is the impact parameter d_0 significance, d_0/σ_{d_0} (see Section 3.2.2 for the definition of d_0). As discussed in Section 4.2, τ leptons usually travel distances of $\sim 1 \text{ mm}$ before decaying, and the τ_h decay products are thus associated with a displaced secondary vertex of production. On the contrary, genuine hadronic jets such as the ones originated by Z (and H) decays are typically produced at the interaction point, hence they tend to have a smaller d_0/σ_{d_0} value.

To compare the d_0 significance for true and fake τ_h s, a sample of 300k $\mu^+\mu^- \rightarrow H\nu_\mu\bar{\nu}_\mu$, $H \rightarrow \tau^+\tau^-$ events (the same that will be used in Section 5.2.1 and is there described in details) was generated with MadGraph5. Figure 4.7 compares the d_0/σ_{d_0} distributions obtained for real τ_h s of the $H \rightarrow \tau^+\tau^-$ sample with the distribution of fake τ_h of the $Z \rightarrow jj$

²“light-flavored jets” here refers to jets originating from the hadronization of u, d or s quarks.

sample. The comparison shows that the d_0/σ_{d_0} can be exploited to significantly reduce the misidentification as τ_h of light-flavored jets, the physics object with the highest fake τ_h rate (5.8%) amongst the ones shown in Table 4.2. The same discrimination based on the d_0 significance can be performed with respect to the fake τ_h s of the $Z \rightarrow e^+e^-$, for the same reason as above.

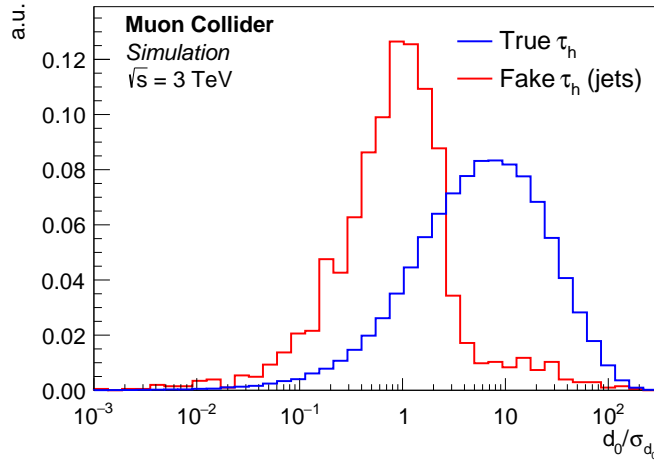


Figure 4.7: Distribution of the impact parameter significance (d_0/σ_{d_0}) for real τ_h s and light-flavored jets misidentified as fake τ_h s. The real τ_h s come from a $H \rightarrow \tau\tau$ sample, while the light-flavored jets from a $Z \rightarrow jj$ sample (see text).

The discrimination of fake τ_h s from b -jets is more challenging. Also b -hadrons typically travel for distances ~ 1 mm before decaying. In this case, the discrimination is usually performed (i) by exploiting the slightly higher decay length of the b -hadrons ($c\tau \approx 490 \mu\text{m}$ for B^\pm mesons) compared to τ leptons ($c\tau \approx 87 \mu\text{m}$), and (ii) by the analysis of additional tracks coming from the τ_h displaced production vertex but not associated with the τ_h candidate.

The implementation of a discrimination technique against fake τ s was out of the scope of this work, but will be a central topic in the future studies of the TAU-FINDER algorithm. Furthermore, more detailed analyses of the misidentification rates as function of p_T and η are certainly desired in the near future.

4.4.4 Tau energy corrections

When the visible products of the τ leptons interact with the detector, they are reconstructed with an energy that can differ from their true energy. This can be due either to statistical fluctuations, e.g. in the interaction with the detector material, or to a bias of the detector systems. To correct this bias, it is possible to study the reconstructed

transverse momentum of the τ visible products vs their MC transverse momentum $p_{T,gen}^{vis}$, in the different decay channels of the τ . The ratio $p_{T,gen}^{vis}/p_{T,reco}^{vis}$, binned in p_T and η , is called τ energy correction. This ratio is crucial in physics studies in which the MC information is not available. Multiplying the reconstructed $p_{T,reco}^{vis}$ (bin by bin) by the jet energy correction, it is possible to estimate the true $p_{T,gen}^{vis}$ of the visible τ decay products.

To compute energy corrections, the τ_h leptons were divided in three classes, by requiring the presence of the following particles both in the reconstructed τ_h jet and in the generator-level decay of the τ : (i) h^\pm with no neutral particles, (ii) h^\pm with at least 1 neutral particle (e.g. a generated π^0 and one or more reconstructed γ or n) and (iii) $h^\pm h^\pm h^\mp$. An example of the energy correction obtained for the categories (i) and (ii) is plotted in Figure 4.8, where it appears clear the importance of separating 1-prong decays with and without the presence of neutrals.

The computation of the energy corrections is propaedeutic for the next chapter, in which they will need to be applied to τ_h leptons from $\mu^+\mu^-$ events to correctly reconstruct the process under investigation, i.e. the Higgs boson decaying into a pair of hadronically decaying τ leptons, $H \rightarrow \tau_h \tau_h$.

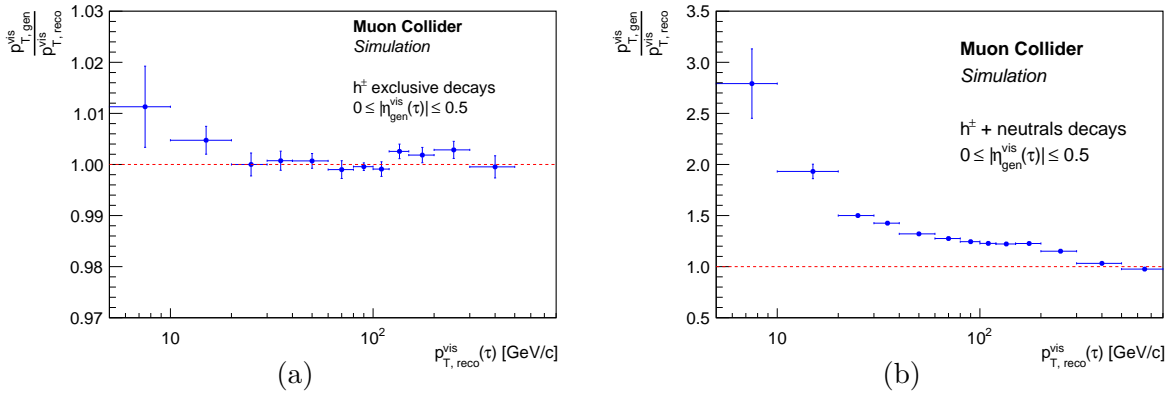


Figure 4.8: Tau energy corrections as a function of the reconstructed p_T of the visible decay products of the τ_h leptons as reconstructed by TAU-FINDER. On the left, the corrections computed for the h^\pm exclusive decays (with no neutrals), on the right the correction computed for the $h^\pm + \text{neutrals}$ decays. In the computation of the corrections, only τ decaying hadronically at generator-level were considered (see text). The τ leptons analyzed are part of the τ particle guns sample detailed in the text.

Chapter 5

$H \rightarrow \tau\tau$ process and cross section measurement

The study of the $H \rightarrow \tau\tau$ decay channel can be used to assess the value of the Higgs boson coupling to τ leptons, to test the consistency of the Standard Model and probe New Physics models. This chapter presents a detailed analysis of the Higgs boson decay into a pair of hadronically decaying τ leptons, $H \rightarrow \tau_h\tau_h$, at a 3 TeV Muon Collider (MuCol). By making use of Boosted Decision Trees (BDTs) for signal-background discrimination and Monte Carlo toy experiments, the statistical uncertainty on the cross section of the $H \rightarrow \tau_h\tau_h$ process is estimated. The reconstruction of the final state τ s is performed with TAU-FINDER, the algorithm described in Chapter 4. For this first analysis, given the challenges met in Chapter 4, the BIB was not included in the event digitisation and reconstruction. A cut on the minimum transverse momentum of the reconstructed τ s, together with a detector acceptance time interval mentioned in Section 3.2.1, partially prepare the path for its insertion in the future. Improvements on the $H \rightarrow \tau\tau$ decay measurement can also be obtained by adding the analysis of other decay channels, such as $\tau_\ell\tau_h$, however they are out of the scope of this work.

5.1 Signal and Background Modeling

The accurate modeling of both the signal and background processes is the foundation of the analysis. As such, this section is dedicated to their detailed description.

5.1.1 Signal process

As reported in Table 2.2, the Higgs boson production at a $\sqrt{s} = 3\text{ TeV}$ $\mu^+\mu^-$ collider proceeds primarily via WW boson fusion (Figure 2.4a). Hence, the signal process is $\mu^+\mu^- \rightarrow H + X$, $H \rightarrow \tau^+\tau^-\nu_\mu\bar{\nu}_\mu$, with two (undetectable) muon neutrinos in the final

state. The cross sections of such process (sketched in Figure 5.1) at $\sqrt{s} = 3 \text{ TeV}$, as given by MadGraph5 [53], is

$$\sigma(\mu^+\mu^- \rightarrow H\nu_\mu\bar{\nu}_\mu, H \rightarrow \tau^+\tau^-) = 30.9 \text{ fb} . \quad (5.1)$$

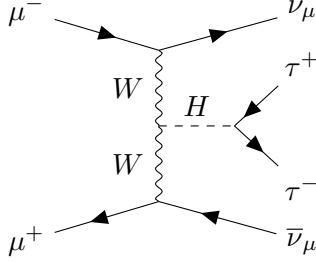


Figure 5.1: Feynman diagram of the signal process under investigation.

The other H production processes, such as the ZZ fusion (Figure 2.4b) and the Higgsstrahlung (Figure 2.4c), bring a minor contribution compared to the WW fusion ($\approx 10\%$ for the ZZ fusion). For future and more exhaustive analyses, they will have to be considered, but in this study they were considered negligible in first approximation, to ease the simulation of the MC samples and the analysis of the kinematical variables.

Multiple neutrinos are present in the signal's final state: two muon neutrinos originated the W^+ and W^- emissions and two tau neutrinos produced in τ leptons decays. Each of the neutrinos carries away a certain amount of undetectable momentum, posing a challenge in the reconstruction of the kinematical variables of both the τ leptons and the H boson (see Section 5.2.2). Indeed, even in presence of an algorithm for missing transverse momentum reconstruction, the Higgs transverse momentum could not be precisely reconstructed, given the undetectable \vec{p}_T^{miss} of the muon neutrinos, making the reconstruction of the tau neutrinos \vec{p}_T^{miss} more challenging.

5.1.2 Background processes

The most significant background processes can be divided in two classes: (i) the inclusive processes $\mu^+\mu^- \rightarrow \tau^+\tau^-\nu_\mu\bar{\nu}_\mu$ and (ii) the inclusive $\mu^+\mu^- \rightarrow \tau^+\tau^-\mu^+\mu^-$, from which the signal processes have to be subtracted. The cross sections at a 3 TeV Muon Collider (excluding the signal process) are the following:

$$\mu^+\mu^- \rightarrow \tau^+\tau^-\nu_\mu\bar{\nu}_\mu = 78.9 \text{ fb} , \quad (5.2)$$

$$\mu^+\mu^- \rightarrow \tau^+\tau^-\mu^+\mu^- = 193 \text{ fb} . \quad (5.3)$$

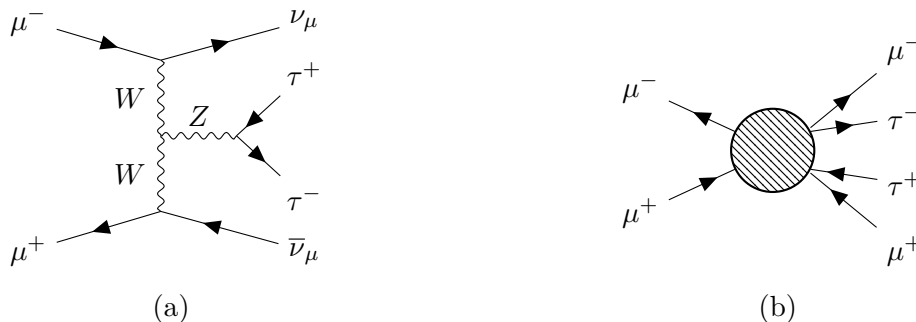


Figure 5.2: Feynman diagrams of the two main background processes in this analysis under investigation (see text). The complete diagrams of the processes contributing to the inclusive $\mu^+\mu^- \rightarrow \mu^+\mu^-\tau^+\tau^-$ (b) are reported in Appendix B.

The category (i) includes the $\mu^+\mu^- \rightarrow Z\nu_\mu\bar{\nu}_\mu$, $Z \rightarrow \tau^+\tau^-$ process, depicted in Figure 5.2a, whose cross section is

$$\sigma(\mu^+\mu^- \rightarrow Z\nu_\mu\bar{\nu}_\mu, Z \rightarrow \tau^+\tau^-) = 73.8 \text{ fb} . \quad (5.4)$$

Comparing the cross sections in Eq. 5.2 and Eq. 5.4, it can be seen that the $\mu^+\mu^- \rightarrow Z\nu_\mu\bar{\nu}_\mu$, $Z \rightarrow \tau^+\tau^-$ contribution is dominant amongst class (i) processes, hence the rest of the processes of this class were in first approximation assumed to be negligible. The discrimination of the $\mu^+\mu^- \rightarrow Z\nu_\mu\bar{\nu}_\mu$, $Z \rightarrow \tau^+\tau^-$ background is particularly challenging, both because it has a larger cross section compared to the signal and because the kinematics of the final state $\tau^+\tau^-$ pair is similar to the one of the signal process, with two important differences: the mass and the spin of the Z ($J = 1$) and H ($J = 0$) bosons.

In the class (ii) processes, sketched in Figure 5.2b, a $\mu^+\mu^-$ pair is present in the final state. Nevertheless, most of the (anti)muons are produced in the forward region, with $|\eta| > 2.44$, escaping the detection system. This holds not only in this case, but for every process in which two Z bosons are emitted from the initial μ^+ and μ^- [71]. The final state detected in the vast majority of this class' processes is $\tau^+\tau^-$, the same as the signal process (the neutrinos are invisible to the detector).

For a conservative analysis, all type (ii) processes were considered as if the muons were not reconstructed, even the ones within the reach of the detection system. A future analysis could instead study the fraction of events in which at least one of the final state muons is reconstructed, and reject those events as they would have a different reconstructed final state with respect to the signal process. The processes belonging to this class are reported in Appendix B.

For simplicity, possible additional backgrounds arising from the presence of fake τ_h leptons in the final state were assumed to be negligible in first approximation, given the small misidentification rates obtained in Section 4.4.3. Future studies of the $H \rightarrow \tau\tau$

decay should also account for these background to provide a complete description of the process.

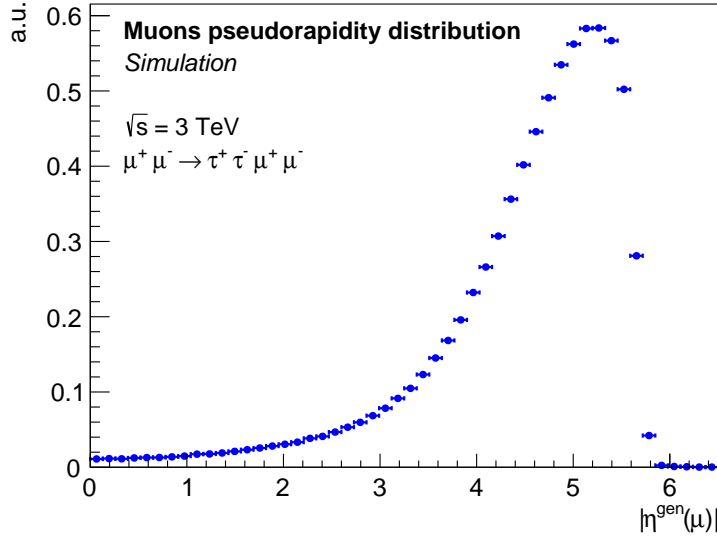


Figure 5.3: Distribution of the pseudorapidity of the final state μ^+ and μ^- in the $\mu^+\mu^- \rightarrow \tau^+\tau^-\mu^+\mu^-$ processes (class (ii) in the text). Most of the muons have $|\eta| > 2.3$, and therefore are not reconstructed with the detector model used in this analysis. The distribution was obtained with the 300k $\mu^+\mu^- \rightarrow \tau^+\tau^-\mu^+\mu^-$ events sample described in the text.

5.2 Signal-background discrimination

Since the total cross section of the background processes is much larger than that of the signal, an optimal signal-to-background ratio is essential to reduce the statistical uncertainty on the signal process' cross section. To do so, it is key to investigate the kinematical variables of the final state $\tau^+\tau^-$ pair.

5.2.1 Sample generation and event selection

To study the kinematical variables of the reconstructed $\tau^+\tau^-$ pair of the background event, samples of the signal and background processes were generated with MadGraph5: 300k signal events, 300k $\mu^+\mu^- \rightarrow Z\nu_\mu\bar{\nu}_\mu$, $Z \rightarrow \tau^+\tau^-$ events and 300k $\mu^+\mu^- \rightarrow \tau^+\tau^-\mu^+\mu^-$ events of inclusive τ decays. The simulation of the detector response, the digitisation and the event reconstruction were performed following the default MuCol workflow described in Section 3.2, with the additional application of TAU-FINDER on the output PF objects. Given the challenges arising in τ leptons reconstruction from the BIB inclusion,

this background was not included in the simulation for this first analysis of the $H \rightarrow \tau\tau$ process with the MuCol software.

After some studies, it was decided to focus the analysis on the $H \rightarrow \tau_h\tau_h$ decay, i.e. on the case of both τ leptons decaying hadronically. The possibility of an analysis including the τ leptonic decay channels (e.g. the $e^\pm + \mu^\mp$ final state) was considered, but it was later discarded because of its reduced signal-background separation, mainly due to the presence of further missing transverse momentum (from the ν_e/ν_μ produced in the τ decays). Such an analysis would also require, as mentioned in Section 4.2, a separation of the τ_l final states from the prompt leptons based on the impact parameter d_0 and its significance.

To understand the characteristics of the samples under study, the kinematical distributions of the final state τ_h s were carefully investigated. The distributions in $|\eta|$ and p_T of the generated τ_h leptons of the $H \rightarrow \tau_h\tau_h$ sample, as well as the distributions in $|\eta^{vis}|$ and p_T^{vis} of the visible decay products of the same τ_h s, are shown in Figure 5.4.

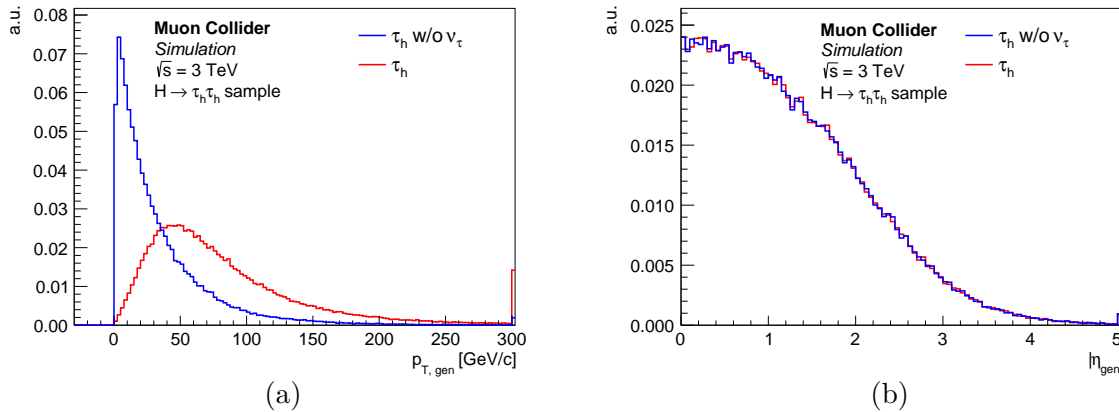


Figure 5.4: Transverse momentum (a) and pseudorapidity (b) distributions of the visible decay products (in blue), i.e. excluding the neutrino, of the generated τ_h leptons from the $H \rightarrow \tau\tau$ sample, for events with two τ_h s (both 1-prong and 3-prong) in the final state. Also shown in red are the transverse momentum and the pseudorapidity of the τ_h before its decay. The last bin of the histograms includes the overflow entries.

A simple event selection was subsequently performed by requiring the presence of exactly two reconstructed τ_h leptons (i.e. with either 1 or 3 reconstructed h^\pm in the jet and no requirements on neutrals) with opposite charges. To suppress soft backgrounds, also in view of the future inclusion of the soft particles of the BIB, a $p_{T,reco}^{vis} > 20$ GeV cut was applied to both τ_h s (after applying the proper energy corrections computed in Section 4.4.4). The efficiencies of the different samples after the event selection are reported in Table 5.1.

Process	Generated events	Events after selection	ϵ	σ [fb]	Expected events (1 ab ⁻¹)
$\mu^+\mu^- \rightarrow H\nu_\mu\bar{\nu}_\mu, H \rightarrow \tau^+\tau^-$	300k	11877	0.04	30.9	1223
$\mu^+\mu^- \rightarrow Z\nu_\mu\bar{\nu}_\mu, Z \rightarrow \tau^+\tau^-$	300k	9008	0.03	73.8	2216
$\mu^+\mu^- \rightarrow \tau^+\tau^-\mu^+\mu^-$	300k	2204	0.007	193	1418

Table 5.1: Number of generated events and events that passed the selection, and the final efficiency ϵ for the signal and the two main background processes. The efficiency is here defined as the number of events that pass the event selection (two reconstructed τ_h s with opposite charges and with $p_{T, reco}^{vis} > 20$ GeV) over the total number of generated events. The estimated cross section at a 3 TeV MuCol is also shown, together with the number of expected events assuming an integrated luminosity of 1 ab⁻¹.

Such low efficiencies, despite the cuts applied are not so stringent, can be motivated. Firstly, the p_T distribution of the reconstructed τ^+ and τ^- displays a shift towards zero when compared to the MC distribution of the true τ lepton p_T , which can be attributed to the presence of undetected missing transverse momentum carried away by neutrinos. Hence, the lower p_T cut is rejecting a significant part of the signal events, as shown in Figure 5.4a, since approximately 50% of the τ_h s in the $H \rightarrow \tau_h\tau_h$ sample have $p_{T, gen} < 20$ GeV/c. The τ_h reconstruction efficiency issues of TAU-FINDER, as discussed in Chapter 4, must also be considered. Additionally, it is important to note that approximately 15% of τ leptons have a pseudorapidity $|\eta| > 2.3$, as shown in Figure 5.4b, and thus cannot be detected. Finally, only 42% of the events considered contain both τ leptons decaying to hadrons, either to 1- or 3-prongs.

In Table 5.1, the expected number of events at a 3 TeV Muon Collider is also shown, computed as

$$N = \epsilon \cdot \sigma \cdot \mathcal{L} , \quad (5.5)$$

where ϵ is the reconstruction efficiency after the event selection (reported in Table 5.1), σ is the cross section of the process and $\mathcal{L} = 1 \text{ ab}^{-1}$ is the integrated luminosity. The results reported in this chapter are all obtained with the same assumption on luminosity.

5.2.2 Boosted Decision Tree

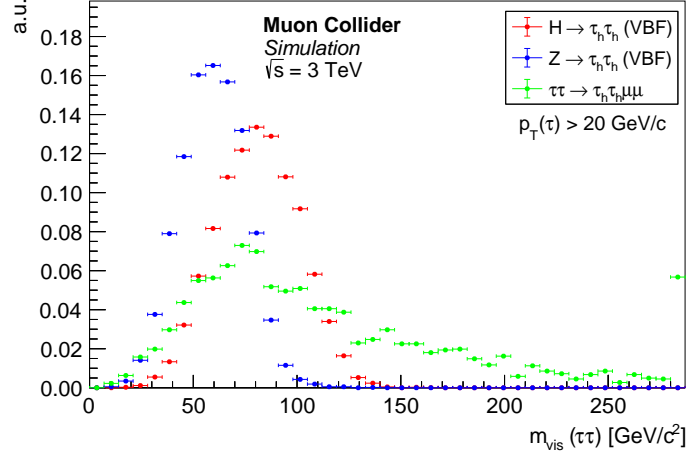
Boosted Decision Trees (BDTs) are a powerful tool in high-energy physics analyses to help in the discrimination between signal and backgrounds, especially when dealing with complex datasets where multiple variables must be considered simultaneously. The TMVA library [72] provides tools to perform multivariate classification with machine learning techniques, in ROOT. In this analysis, TMVA was used to train a BDT using the following set of discriminating variables: the invariant mass of the $\tau_h^+\tau_h^-$ system; the

pseudorapidities η of each τ_h ; the difference $\Delta\phi$ in the azimuthal angles between the τ_h^+ and the τ_h^- ; the transverse momentum p_T of each τ_h . These are variables of interest for the following motivations:

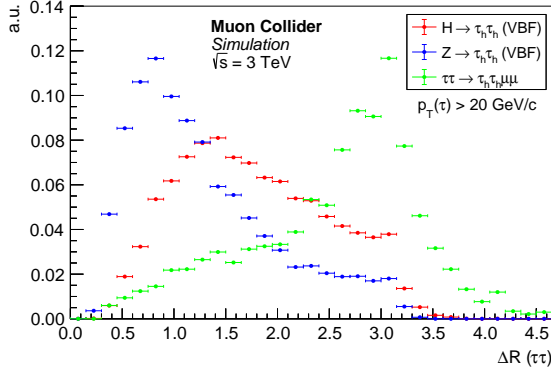
- **Invariant mass of the $\tau^+\tau^-$ system:** This is the most direct variable to distinguish signal and background. If one could reconstruct the whole $\tau^+\tau^-$ system, its distribution would be peaked around m_H in the $H \rightarrow \tau\tau$ events, and peaked around m_Z in the $Z \rightarrow \tau\tau$ events (the other background events would have a more continuous distribution);
- **Angular Distributions:** Since $m_H > m_Z$, and therefore the H boson is averagely produced with a smaller boost than the Z boson, the $\tau^+\tau^-$ pair is expected to have a larger ΔR (i.e. the distance in the $\eta - \phi$ plane between the two τ_h s);
- **Transverse momentum:** The transverse momentum of the $\tau^+\tau^-$ system (and of the single τ_h s) is expected to be lower in H boson events compared to Z boson events, for the same reasons as above.

Since it is only possible to reconstruct the visible products of the $\tau^+\tau^-$ system, and part of the momentum is carried away by the neutrinos, a lower separation is expected to be observed in the signal and background distributions. The invariant mass distributions $m_{vis}(\tau\tau)$, shown in Figure 5.5a, are smeared and shifted towards zero, and the peaks are not centered around the m_Z and m_H values. The ΔR and $p_T(\tau\tau)$ distributions are instead displayed in Figure 5.5b and 5.5c.

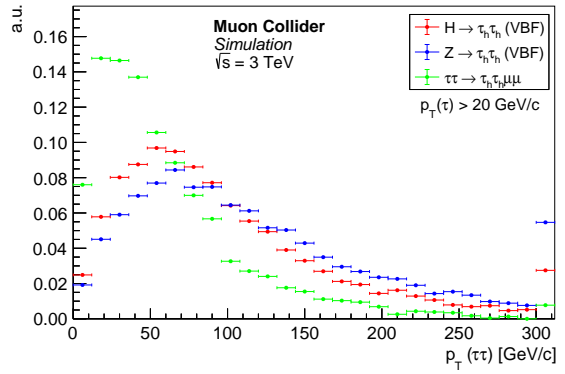
The signal and background reconstructed event samples were split 50-50 into "testing" and "training" samples. The BDT, which employed Adaptive Boost, was trained on the training sample to perform a classification between two types of events: signal and background. The BDT was then run on the testing sample. The output signal and background distributions obtained from the BDT are reported in Figure 5.6 for both the training and testing samples. The BDT output signal and background histograms were properly normalized to the expected number of events at a 3 TeV MuCol, computed according to Eq. 5.5. This procedure allowed to obtain signal and background histogram templates for the fitting. Since no overtraining was detected in the BDT, the whole sample (testing + training) was considered in the computation of the total number of expected events.



(a)



(b)



(c)

Figure 5.5: Invariant mass (a), ΔR (b) and p_T (c) distributions of the reconstructed $\tau_h^+ \tau_h^-$ system, shown separately for the signal and the two backgrounds samples after the event selection. The last bin includes the overflow entries.

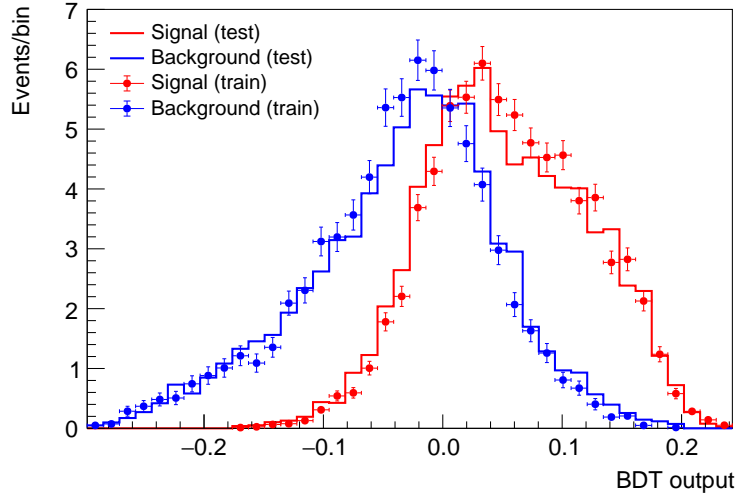


Figure 5.6: Output TMVA BDT histograms for the signal (red) and background (blue) events, split into training and testing samples, showing the performance of the classifier in separating $H \rightarrow \tau_h \tau_h$ from background events. The input events were weighted by TMVA to obtain an equal number of signal and background events, and are not normalized to the expected events at the MuCol.

5.3 Fit procedure and result

Once the templates were obtained, 100k Monte Carlo toy experiments were performed with ROOFIT; in each of these, for each bin a random number from a Poisson distribution with mean equal to the number of events in the bin was extracted, resulting in binned pseudo-data with a meaningful associated uncertainties. For each toy experiment, a combined fit of signal and background templates was performed with ROOFIT, applying no constraints on the signal or background normalization. An example of such fits is shown in Figure 5.7: the normalization of the fitted signal (background) histogram template is equal to the best estimate of the number of signal (background) events in that pseudo-experiment.

The fit provides a direct measurement of the cross section of the signal (in agreement with the expectations), computed as

$$\sigma(H \rightarrow \tau^+ \tau^-) = \frac{N}{\epsilon \cdot \mathcal{L}} . \quad (5.6)$$

Most importantly, by assuming the systematic uncertainties on the efficiency and the luminosity negligible, the absolute statistical uncertainty on the cross section is dominated by the uncertainty on the signal yield. The estimate of the statistical uncertainty $\Delta\sigma$ associated to the signal cross section can be extracted as the standard deviation of the distribution of the signal events in all MC toy experiments. By dividing it by the

cross section of the signal, it is possible to obtain an estimate of the relative statistical uncertainty:

$$\frac{\Delta\sigma(H \rightarrow \tau^+\tau^-)}{\sigma(H \rightarrow \tau^+\tau^-)} = 5.3\% . \quad (5.7)$$

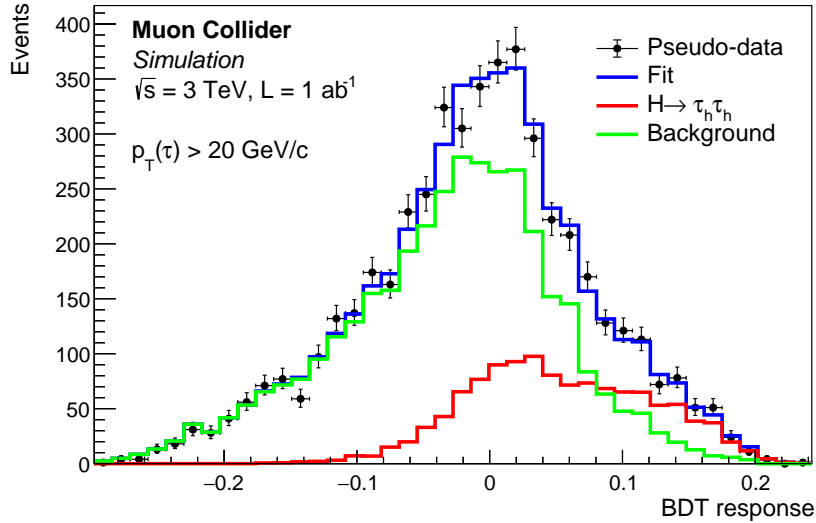


Figure 5.7: Example of a histogram template fit to the pseudo-data (black points) extracted by performing a MC toy experiment on the total BDT response distribution (blue), obtained as a sum of the signal (red) and background (green) BDT output distributions. The total number of events is normalized to the expected number of events at a Muon Collider after the event selection (see Table 5.1).

5.4 Discussion

A meaningful benchmark against which to compare the result is the projection of Ref. [23], computed with the use of DELPHES fast simulation for an equivalent integrated luminosity. The statistical sensitivity on the signal cross section, $H \rightarrow \tau\tau$ via W^+W^- fusion, is reported to be 3.8%. The 5.3% uncertainty is comparable to this projection, also considering the flaws in π^\pm and τ^\pm reconstruction, discussed in Chapter 4. The 3.8% uncertainty was also obtained without the inclusion of the BIB, as in this work.

The results must also be compared with the predicted precision at the other current and future colliders, with the caveat of the exclusion of the BIB. The uncertainty on the $H \rightarrow \tau\tau$ cross section can roughly be compared with the sensitivity on the κ_τ param-

ter¹. The current experimental value of the uncertainty on κ_τ is about 8% [12, 25], as measured by the CMS (see Figure 1.2) and ATLAS experiments. The result obtained proves, with the caveat of the BIB inclusion, that a 3 TeV the Muon Collider can bring a significant contribution to the κ_τ coupling measurement.

The projected sensitivity of the main future colliders on κ_τ is instead shown in Table 1.4: at HL-LHC it is 1.9%, at FCC 0.44%. With the current status of the event reconstruction algorithms, therefore, the 3 TeV MuCol stage would not be able to perform a competitive measurement. Nevertheless, the wide margin for improvement in the event reconstruction and in the $H \rightarrow \tau\tau$ analysis, as will be discussed in the Conclusions and outlook, could lead to a significant enhancement in the precision on the measurement of the $H \rightarrow \tau\tau$ decay channel, and hence on the κ_τ coupling.

¹This comparison is only a coarse approximation, since the uncertainty on κ_τ is usually the result of a 10-parameter fit in the κ -framework.

Conclusions and outlook

This thesis addresses the potential of a 3 TeV Muon Collider in exploring the Higgs sector, with a specific focus on the $H \rightarrow \tau^+\tau^-$ decay channel. Performing precision measurements of the Higgs boson coupling to other SM particles, such as the τ lepton, is fundamental to test the consistency of the Standard Model (SM) and probe the validity of many New Physics theories.

In this work, the performance of the TAU-FINDER algorithm for τ lepton reconstruction at a 3 TeV Muon Collider was assessed, with detailed simulation and event reconstruction carried out with the Muon Collider software MARLIN. To characterize the reconstruction of the charged hadrons produced in τ decays, the charged pion tracking and particle reconstruction performance was studied in different configurations. With this analysis it was shown that, by lowering the hadronic calorimeter energy thresholds from 2 MeV to 250 keV, the algorithm is able to achieve an improved τ_h (a τ lepton decaying into either one or three charged hadrons) reconstruction efficiency, exceeding 60% in the detector central region ($|\eta| < 0.5$) for $10 \text{ GeV}/c \leq p_T \leq 100 \text{ GeV}/c$. TAU-FINDER was then applied to the study of the $H \rightarrow \tau\tau$ decay process. In this first study, only the $H \rightarrow \tau_h\tau_h$ channel, i.e. the Higgs decay into a pair of hadronically decaying τ leptons, was investigated. By employing Monte Carlo toy experiments in combination with a histogram template fit, this study provided a preliminary estimate of the statistical uncertainty achievable on the $H \rightarrow \tau\tau$ cross section at a 3 TeV Muon Collider of $\Delta\sigma/\sigma = 5.3\%$. This value is comparable to the one reported in previous studies done with DELPHES fast detector simulation (3.8%), but is still distant from the projected precision of HL-LHC (1.9%) and FCC (0.4%) on the κ_τ coupling modifier. However, the estimate obtained is only a first, preliminary assessment, as many improvements are already in progress.

The results presented in this work come with an important caveat, that is to say the exclusion from the analysis of the beam-induced background (BIB) generated by the decays of the muons. Since the BIB consists of soft, out-of-time particles, some strategies and cuts are employed to partly account for its presence. Hence, this work paves the path for the inclusion of such background in the study, a key step in the advancement in the understanding of τ identification and of the $H \rightarrow \tau\tau$ process.

There is room for improvement in the event reconstruction and in the $H \rightarrow \tau\tau$ analysis. The τ_h reconstruction efficiency can be enhanced. The major flaws are residing in the PandoraPFA algorithm, which is not able to correctly associate the tracks with the calorimeter clusters for charged pions. The resulting drops in τ_h efficiency are responsible of a poor efficiency in the $H \rightarrow \tau_h\tau_h$ decay channel. A detailed investigation of the cause of such flaws must be a priority of the next upgrades of the MARLIN software, together with the correction of the drops in the tracking efficiency obtained using the Combinatorial Kalman Filter (CKF) tracking algorithm.

As stated above, the beam-induced background needs to be included in the analysis. To do so, an optimal configuration for the calorimeter thresholds, designed to balance efficiency and computational performance, has to be studied: the whole analysis was performed with the adapted threshold of 250 keV for the HCAL, which is not the default for the Muon Collider detector. The determination of the optimal thresholds should be performed with a 3 TeV BIB sample and with the nozzles' configuration optimized for this center-of-mass energy.

The TAU-FINDER algorithm could be adjusted, for example by testing the effects of changing the opening angle of the signal and isolation cones, or by modifying other cuts to search for the configuration which best suits the Muon Collider. Alternatively, a new algorithm for τ reconstruction and identification could be developed, which should account for the presence of the soft BIB particles in the event.

The $H \rightarrow \tau\tau$ analysis can be extended to include the τ leptonic decay channels, upon a detailed analysis of the impact parameter d_0 to separate the final state e/μ from prompt leptons. The analysis could also be refined with the inclusion of the $\mu^+\mu^- \rightarrow H\mu^+\mu^-$, $H \rightarrow \tau^+\tau^-$ signal process and a detailed study of the events with fake τ_h s.

The development of a system for the tagging of the forward muons (up to $|\eta| = 7$) is one of the IMCC collaboration's top priorities [28]. This would allow not only to detect the forward muons to distinguish ZZ and WW fusion final states, but particularly to reject a significant fraction of the $\mu^+\mu^- \rightarrow \tau^+\tau^-\mu^+\mu^-$ events, which constitute a major background in the analysis.

The ultimate step to grasp the real potential of the Muon Collider will be the study of the $H \rightarrow \tau\tau$ process at a 10 TeV center-of-mass energy, the final stage foreseen in the IMCC program.

In conclusion, this thesis highlights the 3 TeV Muon Collider's potential to advance our understanding of the Higgs boson and its coupling to τ leptons. These findings contribute to the ongoing effort to probe the effectiveness of the Muon Collider as a tool in investigating New Physics, and at the same time enhance the understanding of the strengths and weaknesses of the Muon Collider software MARLIN and its event reconstruction algorithms, clearing the way towards Higgs boson measurements with unprecedented precision.

Appendix A

Tau lepton reconstruction and identification at the CMS experiment

In this appendix, the algorithms for τ lepton reconstruction and identification used at the CMS experiment are discussed.

A.1 Tau reconstruction at CMS

At CMS, the reconstruction of τ_h candidates is performed with the hadrons-plus-strips algorithm [73], while the τ_h identification is performed by DEEPTAU [64].

The hadrons-plus-strips reconstruction proceeds in four steps, summarized as follows:

1. τ_h seed regions are defined by reconstructed hadronic jets. The jets for the seeding are clustered from all particles reconstructed by a PF algorithm [74] using the anti- k_T algorithm with a distance parameter of $R = 0.4$. All particles in an $\eta - \phi$ cone of radius $\Delta R \equiv \sqrt{(\Delta\eta)^2 + (\Delta\phi)^2} = 0.5$ around the jet axis are considered for the next steps of the τ_h reconstruction.
2. π_0 candidates are then reconstructed using “strips” in $\eta - \phi$ plane, in which the four-momenta of electrons and photons are added, and charged hadron (h^\pm) candidates are selected amongst the PF charged particles.
3. All possible τ_h candidates are reconstructed in the different τ hadronic decay modes from the reconstructed h^\pm and strips. The final τ_h four-momentum is computed summing the four-momenta of the h^\pm s and strips used to reconstruct the candidate.
4. The τ_h candidate with the highest p_T is chosen among all possible reconstructed candidates within a seed region.

Additionally, the τ_h candidates must satisfy the following constraints:

1. In case of a decay mode involving a resonance (see Table 4.1), the mass of the τ_h is required to be (loosely) compatible with the mass spectrum expected (including the possible resonance);
2. The τ_h charge must be equal to ± 1 ;
3. All reconstructed h^\pm and π^0 need to be in the signal cone, defined with radius $\Delta R = 3.0/p_T(\text{GeV})$ (with $0.05 \leq \Delta R \leq 0.1$) with respect to the τ_h momentum direction.

The τ_h candidates reconstructed by this algorithm, together with their low-level and high-level information, are then passed to the ID algorithm to be discriminated against quark or gluon jets, electrons, and muons.

A.2 Hadronic tau identification at CMS

DEEPTAU [64] is a deep neural network (DNN)-based algorithm for τ_h identification at CMS. It is able to simultaneously reject e, μ and hadronic jets reconstructed as a τ_h candidate, based on both tree ensembles and selection criteria. Compared to its Multivariate Analysis (MVA) predecessors, it uses lower-level inputs, but still 47 high-level input variables are used, to reduce the number of training events needed and improve the convergence of the training. Example of the high-level variables are the τ_h four-momentum, its charge, the number of charged and neutral particles used to reconstruct the candidate, the estimated pileup density in the event.

The deep neural network requires a partitioning of the inputs. Indeed, two overlapping two-dimensional grids in the $\eta - \phi$ plane, centered around the τ_h axis, are defined: a central inner grid, with a finer cell size, and an wider grid, with a coarser cell size. As it can be noted in sketch of the two grids, depicted in Figure A.1, the coarser grid includes a large area outside the signal cone. This is because the DNN input variables include information about the objects reconstructed in an isolation cone around the signal cone, to help the discrimination of τ_h against genuine hadronic jets.

For each grid cell, the properties of the reconstructed particles of different types contained within it are used as inputs. For each type of reconstructed particle (e.g. muons, electrons, photons, charged hadrons, neutral hadrons), different variables are used; if there are two or more particles of the same type in the same cell, only the one with the highest p_T is considered.

Information from inner cells and outer cells, together with some high-level variables, is fed into the DNN. The DNN processes all the inputs from a τ_h candidate to yield as

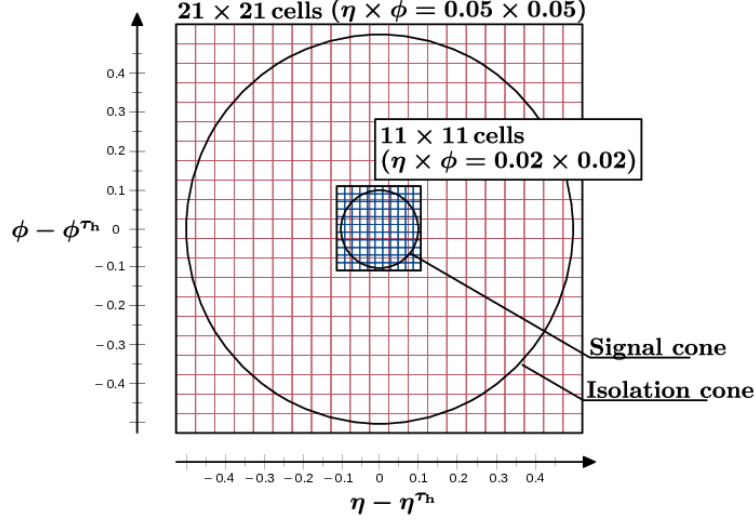


Figure A.1: Graphical visualization of the grids in $\eta - \phi$ space used for the reconstruction algorithm. The finer inner grid and the coarser outer grid are centered around the axis of the reconstructed τ_h . The signal and isolation cones used in the algorithm are also shown. From Ref. [64].

output the estimates y_α ($y_e, y_\mu, y_\tau, y_{\text{jet}}$) of the probabilities of the candidate to belong to one of the four target classes $e, \mu, \tau_h, \text{jet}$. The final discriminators against electrons, muons and jets are given by

$$D_\alpha = \frac{y_\tau}{y_\tau + y_\alpha} \quad , \quad \text{with } \alpha \in \{e, \mu, \text{jet}\} . \quad (\text{A.1})$$

The final τ_h ID efficiency, evaluated on samples simulated according to the CMS data-taking conditions, are reported in Figure A.2 for different working points of the discriminators, as a function of the τ p_T (Figure A.2a) and against the mis-identification probabilities (Figure A.2b).

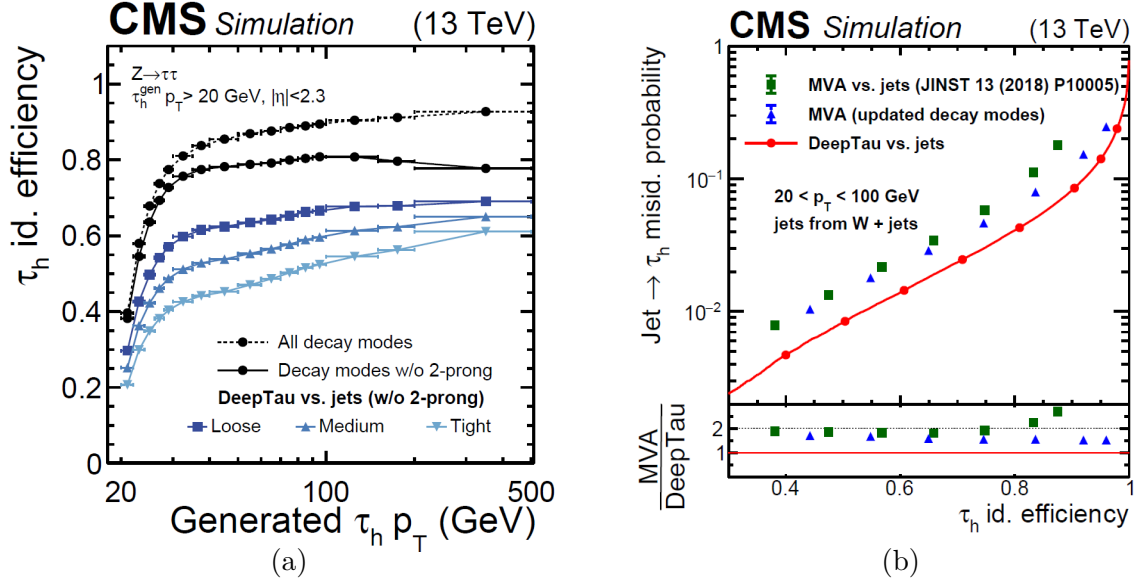
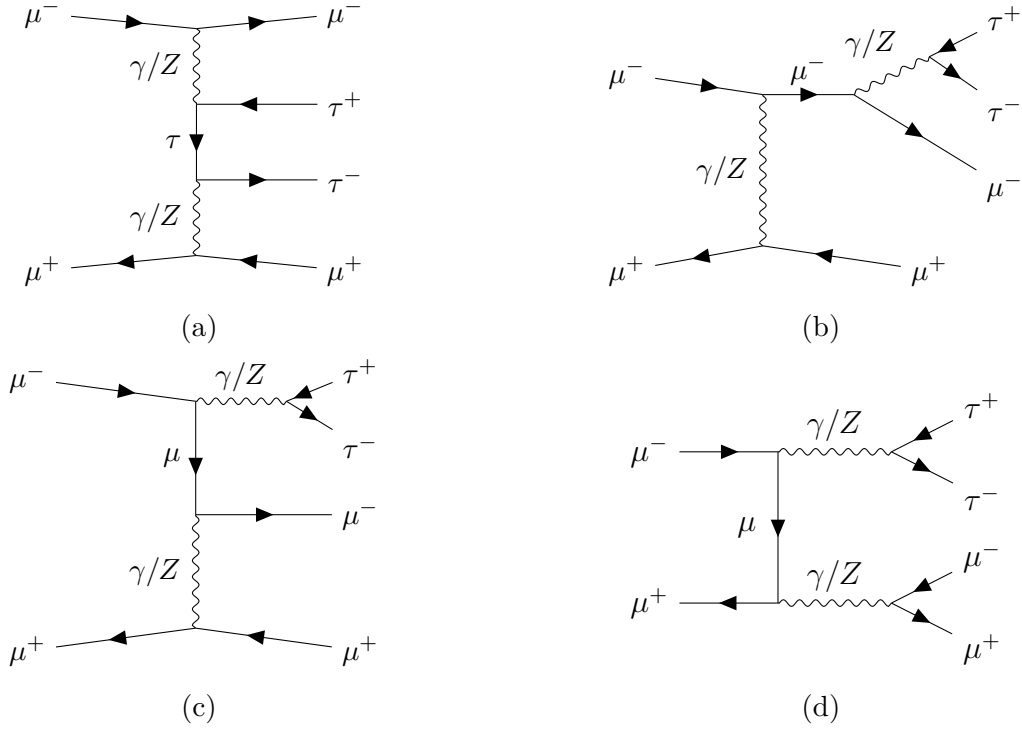


Figure A.2: (a) Efficiencies for simulated τ_h s with $|\eta| < 2.3$ to be correctly reconstructed and identified as τ_h s with $p_T > 20$ GeV, shown as a function of the true visible p_T for different identification criteria ("working points"). The black dashed line represents τ_h s reconstructed in any decay mode (including those with missing charged hadrons), while the solid black line excludes modes with missing charged hadrons. Blue lines show the efficiency for τ_h s passing the Loose, Medium, or Tight D_{jet} discriminator working points. The τ_h s come from $Z \rightarrow \tau\tau$ events. (b) Efficiency of simulated τ_h identification (with $20 < p_T < 100$ GeV) versus the probability of a genuine hadronic jet (with $20 < p_T < 100$ GeV) being misidentified as a τ_h . Red points show DEEPTAU performance across various D_{jet} discriminator working points (VVTight to VVVLoose), while green and blue points represent the performance of the previous MVA algorithms used at CMS. The hadronic jets are from a W +jets sample. Adapted from Ref. [64].

Appendix B

Background processes diagrams

As briefly discussed in Chapter 5, the $\mu^+\mu^- \rightarrow \tau^+\tau^-\mu^+\mu^-$ processes, with a total cross section of 193 fb (see Eq. 5.3), was treated as a background in this analysis. This is because this class of processes can mimic the final state of the $\mu^+\mu^- \rightarrow H\nu_\mu\bar{\nu}_\mu$, $H \rightarrow \tau^+\tau^-$ signal process, since most of the muons are produced with $|\eta| > 2.3$ (see Figure 5.4b), and are therefore not detectable with the current experimental apparatus. The diagrams contributing to this final state, as given by MadGraph5 [53], are reported in Figure B.1.



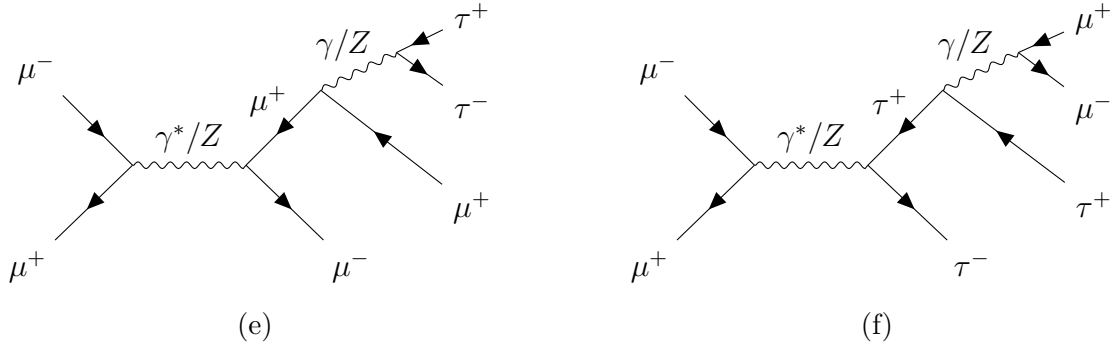


Figure B.1: Feynman diagrams of the processes contributing to the $\tau^+\tau^-\mu^+\mu^-$ final state, as given by MadGraph5. The processes that can be obtained by simply substituting in the diagram a μ^+ with a μ^- (and viceversa) are omitted.

Bibliography

- [1] P.W. Higgs. “Broken Symmetries and the Masses of Gauge Bosons”. In: *Phys. Rev. Lett.* 13 (16 Oct. 1964), pp. 508–509. DOI: 10.1103/PhysRevLett.13.508.
- [2] CMS Collaboration. “Observation of a new boson at a mass of 125 GeV with the CMS experiment at the LHC”. In: *Physics Letters B* 716.1 (2012), pp. 30–61. DOI: 10.1016/j.physletb.2012.08.021.
- [3] ATLAS Collaboration. “Observation of a new particle in the search for the Standard Model Higgs boson with the ATLAS detector at the LHC”. In: *Physics Letters B* 716.1 (2012), pp. 1–29. DOI: 10.1016/j.physletb.2012.08.020.
- [4] D.E. Soper. “Parton distribution functions”. In: *Nuclear Physics B - Proceedings Supplements* 53.1 (1997). Lattice 96, pp. 69–80. DOI: 10.1016/S0920-5632(96)00600-7.
- [5] R.L. Workman et al. “Review of Particle Physics”. In: *PTEP* 2022 (2022), p. 083C01. DOI: 10.1093/ptep/ptac097.
- [6] CERN. *Handbook of LHC Higgs Cross Sections: 1. Inclusive Observables*. en. 2011. DOI: 10.5170/CERN-2011-002.
- [7] CERN. *Handbook of LHC Higgs Cross Sections: 3. Higgs Properties: Report of the LHC Higgs Cross Section Working Group*. en. 2013. DOI: 10.5170/CERN-2013-004.
- [8] CERN. *Handbook of LHC Higgs cross sections: 4. Deciphering the nature of the Higgs sector*. en. 2017. DOI: 10.23731/CYRM-2017-002.
- [9] ATLAS Collaboration. “Combined Measurement of the Higgs Boson Mass from the $H \rightarrow \gamma\gamma$ and $H \rightarrow ZZ^* \rightarrow 4\ell$ Decay Channels with the ATLAS Detector Using $\sqrt{s} = 7, 8$, and 13 TeV pp Collision Data”. In: *Phys. Rev. Lett.* 131 (25 Dec. 2023), p. 251802. DOI: 10.1103/PhysRevLett.131.251802.
- [10] CMS Collaboration. *Measurement of the Higgs boson mass and width using the four leptons final state*. Geneva: CERN, 2023. URL: <https://cds.cern.ch/record/2871702>.
- [11] A. Azatov et al. *Off-shell Higgs Interpretations Task Force: Models and Effective Field Theories Subgroup Report*. Mar. 2022. DOI: 10.17181/LHCHWG-2022-001.

- [12] CMS collaboration. “A portrait of the Higgs boson by the CMS experiment ten years after the discovery”. In: *Nature* 607.7917 (July 2022), pp. 60–68. DOI: 10.1038/s41586-022-04892-x.
- [13] ATLAS collaboration. “Constraints on the Higgs boson self-coupling from single- and double-Higgs production with the ATLAS detector using pp collisions at $\sqrt{s} = 13$ TeV”. In: *Physics Letters B* 843 (Aug. 2023), p. 137745. DOI: 10.1016/j.physletb.2023.137745.
- [14] CMS Collaboration. *Constraints on the Higgs boson self-coupling from the combination of single and double Higgs boson production in proton-proton collisions at $\sqrt{s} = 13$ TeV*. 2024. arXiv: 2407.13554 [hep-ex].
- [15] B. Patt and F. Wilczek. *Higgs-field Portal into Hidden Sectors*. May 2006. arXiv: hep-ph/0605188 [hep-ph].
- [16] G. Degrandi et al. “Higgs mass and vacuum stability in the Standard Model at NNLO”. In: *Journal of High Energy Physics* 2012.8 (Aug. 2012). DOI: 10.1007/jhep08(2012)098.
- [17] G. Apollinari et al. *High Luminosity Large Hadron Collider HL-LHC*. en. 2015. DOI: 10.5170/CERN-2015-005.1.
- [18] FCC Collaboration. “FCC Physics Opportunities: Future Circular Collider Conceptual Design Report Volume 1”. In: *Eur. Phys. J. C* 79.6 (2019), p. 474. DOI: 10.1140/epjc/s10052-019-6904-3.
- [19] The CEPC Study Group. *CEPC Technical Design Report - Accelerator (v2)*. 2023. arXiv: 2312.14363 [physics.acc-ph].
- [20] Linear Collider Collaboration. *The International Linear Collider: A Global Project*. 2019. arXiv: 1903.01629 [hep-ex].
- [21] CLIC and CLICdp collaborations. *CERN Yellow Reports: Monographs, Vol 2 (2018): The Compact Linear e^+e^- Collider (CLIC) : 2018 Summary Report*. en. 2018. DOI: 10.23731/CYRM-2018-002.
- [22] J. de Blas et al. “Higgs Boson studies at future particle colliders”. In: *Journal of High Energy Physics* 2020.1 (Jan. 2020). DOI: 10.1007/jhep01(2020)139.
- [23] M. Forslund and P. Meade. “High precision higgs from high energy muon colliders”. In: *Journal of High Energy Physics* 2022.8 (Aug. 2022). DOI: 10.1007/jhep08(2022)185.
- [24] J. de Favereau et al. “DELPHES 3: a modular framework for fast simulation of a generic collider experiment”. In: *Journal of High Energy Physics* 2014.2 (Feb. 2014). DOI: 10.1007/jhep02(2014)057.

- [25] ATLAS collaboration. “A detailed map of Higgs boson interactions by the ATLAS experiment ten years after the discovery”. In: *Nature* 607.7917 (July 2022), pp. 52–59. DOI: 10.1038/s41586-022-04893-w.
- [26] S. Vita et al. “A global view on the Higgs self-coupling at lepton colliders”. In: *Journal of High Energy Physics* 2018 (Nov. 2017). DOI: 10.1007/jhep02(2018)178.
- [27] A. Taliencio et al. *Higgs Self Couplings Measurements at Future proton-proton Colliders: a Snowmass White Paper*. Mar. 2022. arXiv: 2203.08042 [hep-ex].
- [28] C. Accettura et al. “Towards a Muon Collider”. In: *Eur. Phys. J. C* 83.9 (2023). [Erratum: *Eur.Phys.J.C* 84, 36 (2024)], p. 864. DOI: 10.1140/epjc/s10052-023-11889-x.
- [29] Muon Collider Collaboration. “The International Muon Collider Collaboration”. In: *JACoW*. Vol. IPAC2021. 2021, pp. 3792–3795. DOI: 10.18429/JACoW-IPAC2021-THPAB017.
- [30] H. Al Ali et al. “The muon smasher’s guide”. In: *Reports on Progress in Physics* 85.8 (July 2022), p. 084201. DOI: 10.1088/1361-6633/ac6678.
- [31] M. Casarsa et al. “Higgs physics prospects at a 3 TeV muon collider”. In: *PoS*. Vol. EPS-HEP2023. 2024, p. 408. DOI: 10.22323/1.449.0408.
- [32] C. Accettura et al. *Interim report for the International Muon Collider Collaboration (IMCC)*. July 2024. arXiv: 2407.12450 [physics.acc-ph].
- [33] Y. Torun et al. “The US Muon Accelerator Program”. In: *Conf.Proc.C100523:3491-3493, 2010*. May 2010. URL: <https://www.osti.gov/biblio/988910>.
- [34] M. Bogomilov et al. “Demonstration of cooling by the Muon Ionization Cooling Experiment”. In: *Nature* 578 (Feb. 2020), pp. 53–59. DOI: 10.1038/s41586-020-1958-9.
- [35] M. Otani. “Cool as muons”. In: *Nature Physics* (July 2024). DOI: 10.1038/s41567-024-02571-4.
- [36] T.A. Mohayai et al. “A Wedge Test in MICE”. In: *9th International Particle Accelerator Conference*. June 2018. DOI: 10.18429/JACoW-IPAC2018-TUPML062.
- [37] D. Arominski et al. *A detector for CLIC: main parameters and performance*. 2018. arXiv: 1812.07337 [physics.ins-det].
- [38] N. Bartosik et al. *Simulated Detector Performance at the Muon Collider*. Mar. 2022. arXiv: 2203.07964 [hep-ex].
- [39] N.V. Mokhov and S.I. Striganov. “Detector Backgrounds at Muon Colliders”. In: *Physics Procedia*. Vol. 37. Proceedings of the 2nd International Conference on Technology and Instrumentation in Particle Physics (TIPP 2011). 2012, pp. 2015–2022. DOI: 10.1016/j.phpro.2012.03.761.

- [40] D. Lucchesi et al. “Machine-Detector interface for multi-TeV Muon Collider”. In: *PoS*. Vol. EPS-HEP2023. 2024, p. 630. DOI: 10.22323/1.449.0630.
- [41] G. Da Molin. “Study of b- and c- jets identification for Higgs coupling measurement at muon collider”. MA thesis. UniPD, 2020. URL: <https://hdl.handle.net/20.500.12608/3238>.
- [42] S. Ceravolo et al. “Crilin: A CRystal calorImeter with Longitudinal Information for a future Muon Collider”. In: *Nucl. Instrum. Methods Phys. Res. A* 1047 (2023), p. 167817. DOI: 10.1016/j.nima.2022.167817.
- [43] N.V. Mokhov and C.C. James. *The MARS Code System User’s Guide Version 15(2016)*. Feb. 2017. DOI: 10.2172/1462233.
- [44] C. Ahdida et al. “New Capabilities of the FLUKA Multi-Purpose Code”. English. In: *Frontiers in Physics* 9 (Jan. 2022). DOI: 10.3389/fphy.2021.788253.
- [45] G. Battistoni et al. “Overview of the FLUKA code”. In: *Annals of Nuclear Energy* 82 (2015), pp. 10–18. DOI: 10.1016/j.anucene.2014.11.007.
- [46] *Muon Collider software GitHub folder*. URL: <https://github.com/MuonColliderSoft>.
- [47] *ILCsoftware web page*. URL: <https://ilcsoft.desy.de/portal/>.
- [48] M Frank et al. “DD4hep: A Detector Description Toolkit for High Energy Physics Experiments”. In: *Journal of Physics: Conference Series* 513.2 (June 2014), p. 022010. DOI: 10.1088/1742-6596/513/2/022010.
- [49] S. Agostinelli et al. “Geant4—a simulation toolkit”. In: *Nucl. Instrum. Methods Phys. Res. A* 506.3 (2003), pp. 250–303. DOI: 10.1016/S0168-9002(03)01368-8.
- [50] J. Allison et al. “Geant4 Developments and Applications”. In: *IEEE Transactions on Nuclear Science* 53 (Feb. 2006), pp. 270–278. DOI: 10.1109/TNS.2006.869826.
- [51] J. Allison et al. “Recent developments in Geant4”. In: *Nucl. Instrum. Methods Phys. Res. A* 835 (2016), pp. 186–225. DOI: 10.1016/j.nima.2016.06.125.
- [52] F. Gaede. “Marlin and LCCD—Software tools for the ILC”. In: *Nucl. Instrum. Methods Phys. Res. A* 559.1 (2006). Proceedings of the X International Workshop on Advanced Computing and Analysis Techniques in Physics Research, pp. 177–180. DOI: 10.1016/j.nima.2005.11.138.
- [53] J. Alwall et al. “MadGraph 5: Going Beyond”. In: *JHEP* 06 (2011), p. 128. DOI: 10.1007/JHEP06(2011)128.
- [54] A. Mereghetti et al. “The FLUKA LineBuilder and Element DataBase: Tools for Building Complex Models of Accelerator Beam Lines”. In: *Conf.Proc.* Vol. C1205201. Jan. 2012, pp. 2687–2689.

- [55] E. Brondolin et al. “Conformal tracking for all-silicon trackers at future electron–positron colliders”. In: *Nucl. Instrum. Methods Phys. Res. A* 956 (2020), p. 163304. DOI: 10.1016/j.nima.2019.163304.
- [56] M. Hansroul, H. Jeremie, and D. Savard. “Fast circle fit with the conformal mapping method”. In: *Nucl. Instrum. Methods Phys. Res. A* 270.2 (1988), pp. 498–501. DOI: 10.1016/0168-9002(88)90722-X.
- [57] A. Glazov et al. “Filtering tracks in discrete detectors using a cellular automaton”. In: *Nucl. Instrum. Methods Phys. Res. A* 329.1 (1993), pp. 262–268. DOI: 10.1016/0168-9002(93)90945-E.
- [58] R.E. Kalman. “A New Approach to Linear Filtering and Prediction Problems”. In: *Journal of Basic Engineering* 82.1 (Mar. 1960), pp. 35–45. DOI: 10.1115/1.3662552.
- [59] X. Ai et al. “A Common Tracking Software Project”. In: *Computing and Software for Big Science* 6.1 (Apr. 2022). DOI: 10.1007/s41781-021-00078-8.
- [60] *ACTS documentation*. URL: <https://acts.readthedocs.io/en/latest/tracking.html>.
- [61] J.S. Marshall and M.A. Thomson. *Pandora Particle Flow Algorithm*. 2013, pp. 305–315. arXiv: 1308.4537 [physics.ins-det].
- [62] M.A. Thomson. “Particle flow calorimetry and the PandoraPFA algorithm”. In: *Nucl. Instrum. Methods Phys. Res. A* 611.1 (Nov. 2009), pp. 25–40. DOI: 10.1016/j.nima.2009.09.009.
- [63] J.S. Marshall, A. Münnich, and M.A. Thomson. “Performance of particle flow calorimetry at CLIC”. In: *Nucl. Instrum. Methods Phys. Res. A* 700 (Feb. 2013), pp. 153–162. DOI: 10.1016/j.nima.2012.10.038.
- [64] CMS collaboration. “Identification of hadronic tau lepton decays using a deep neural network”. In: *Journal of Instrumentation* 17.07 (July 2022), P07023. DOI: 10.1088/1748-0221/17/07/P07023.
- [65] M.L. Perl et al. “Evidence for Anomalous Lepton Production in e^+e^- Annihilation”. In: *Phys. Rev. Lett.* 35 (22 Dec. 1975), pp. 1489–1492. DOI: 10.1103/PhysRevLett.35.1489.
- [66] M. Grunewald. “Tau physics at LEP”. In: *Physica Scripta* 53 (1996), pp. 257–290. URL: <https://api.semanticscholar.org/CorpusID:123106508>.
- [67] M. Capeans et al. *ATLAS Insertable B-Layer Technical Design Report. CERN-LHCC-2010-013, ATLAS-TDR-19*. Sept. 2010.
- [68] The Tracker Group of the CMS Collaboration. *The CMS Phase-1 Pixel Detector Upgrade*. 2020. arXiv: 2012.14304 [physics.ins-det].

- [69] *LCTuple package GitHub folder*. URL: <https://github.com/iLCSoft/LCTuple>.
- [70] A Muennich. *TauFinder: A Reconstruction Algorithm for τ Leptons at Linear Colliders*. 2010. URL: <https://cds.cern.ch/record/1443551>.
- [71] M. Ruhdorfer, E. Salvioni, and A. Wulzer. “Invisible Higgs boson decay from forward muons at a muon collider”. In: *Physical Review D* 107.9 (May 2023). DOI: 10.1103/physrevd.107.095038.
- [72] Andreas Hocker et al. *TMVA - Toolkit for Multivariate Data Analysis*. Mar. 2007. arXiv: physics/0703039.
- [73] CMS Collaboration. “Performance of reconstruction and identification of τ leptons decaying to hadrons and ν_τ in pp collisions at $\sqrt{s} = 13$ TeV”. In: *Journal of Instrumentation* 13.10 (Oct. 2018), P10005–P10005. DOI: 10.1088/1748-0221/13/10/p10005.
- [74] CMS Collaboration. “Particle-flow reconstruction and global event description with the CMS detector”. In: *Journal of Instrumentation* 12.10 (Oct. 2017), P10003–P10003. DOI: 10.1088/1748-0221/12/10/p10003.

Acknowledgements (Ringraziamenti)

I gratefully acknowledge the financial support provided by the EU project “MuCol HORIZON-INFRA-2022-DEV-01-01”, which funded my internship at LIP.

Un ringraziamento va al prof. Gallinaro e al prof. Sioli per avermi accompagnato lungo questo percorso, e specialmente a Giacomo Da Molin e Giovanni Marozzo, senza i quali questa tesi non avrebbe mai visto la luce.

Grazie ai miei familiari, per la vostra curiosità verso il mio lavoro e il supporto prezioso. Grazie a tutti i compagni e tutte le compagne che ho avuto accanto durante questi anni, per le colazioni, i pranzi, i caffè, le cene, le risate, i momenti di sconforto, le gioie, le pacche sulle spalle durante il mio percorso.

Grazie a mia madre, che mi ha insegnato a guardare il mondo con semplicità e ad amare gratuitamente.

Grazie a mio padre, che con la sua presenza silenziosa mi ha mostrato la costanza e l'impegno.

Grazie a Francesco, che mi ha trasmesso la passione per la scienza, con le sue spiegazioni fin da quando andavo alle elementari.

Grazie a Maria, che mi ha insegnato ad amare quello che faccio, con uno sguardo verso chi non può farlo.

Grazie a Ilaria per esserci stata sempre.